Quantum Dot-based Tandem Photodiodes for High-Efficiency Photo-Stimulation in Biomedical Applications

by

Parsa Kaviani

A Dissertation Submitted to the
Graduate School of Sciences and Engineering
in Partial Fulfillment of the Requirements for
the Degree of

Master of Science

in

Electrical and Electronics Engineering

KOÇ ÜNİVERSİTESİ

December 26, 2025

Quantum Dot-based Tandem Photodiodes for High-Efficiency Photo-Stimulation in Biomedical Applications

Koç University

Graduate School of Sciences and Engineering

This is to certify that I have examined this copy of a master's thesis by

Parsa Kaviani

and have found that it is complete and satisfactory in all respects,
and that any and all revisions required by the final
examining committee have been made.

Committee Members:

_____

Prof. Sedat Nizamoğlu (Advisor)

_____

Prof. Alphan Sennaroğlu

_____

Assoc. Prof. Mahmut Emin Çelik

Date: _____

To my lovely family and my dearest Parmida

ABSTRACT

Quantum Dot-based Tandem Photodiodes for High-Efficiency Photo-Stimulation in Biomedical Applications
Parsa Kaviani
Master of Science in Electrical and Electronics Engineering
December 26, 2025

Photovoltaic retinal prostheses offer a promising solution for restoring vision in individuals with degenerative retinal diseases through light-mediated neural stimulation. Colloidal quantum dots (QDs), particularly silver bismuth sulfide ($AgBiS_2$), provide advantages for bioelectronic interfaces due to their high NIR absorption, chemical stability, and non-toxicity. Tandem photovoltaic structures are known to enhance performance by increasing the open-circuit voltage (Voc). We introduce a novel QD-based tandem photodiode, featuring ultra-thin $AgBiS_2$ layers in both subcells. The device generates capacitive photocurrent, and due to the higher Voc, it injects higher ionic charge compared to non-tandem counterparts. The biointerfaces demonstrate low in vitro toxicity and stable photoelectrical performance under various tests. These results highlight the potential of this QD-based tandem photodiode as a high-resolution, efficient, and safe platform for retinal stimulation, offering a flexible, scalable solution for bioelectronic interfaces.

ÖZETÇE

Biyomedikal Uygulamalarda Yüksek Verimli Foto-Uyarım için Kuantum Nokta Tabanlı Tandem Fotodiyotlar

Parsa Kaviani

Elektrik ve Elektronik Mühendisliği, Yüksek Lisans

26 Aralik 2025

Fotovoltaik retinal protezler, ışık aracılı sinirsel uyarı yoluyla dejeneratif retina hastalıklarına sahip bireylerde görmeyi yeniden kazandırmak için umut vadeden bir çözüm sunmaktadır. Kolloidal kuantum noktaları (QDs), özellikle gümüş bizmut sülfür ($AgBiS_2$), yüksek NIR soğurumu, kimyasal kararlılığı ve toksik olmaması nedeniyle bioelektronik ara yüzler için önemli avantajlar sağlamaktadır.

Tandem fotovoltaik yapılar, açık devre gerilimini (V_{OC}) artırarak performansı geliştirmeleriyle bilinmektedir. Bu çalışmada, her iki alt hücrede ultra ince $AgBiS_2$ katmanları içeren yenilikçi bir kuantum nokta tabanlı tandem fotodiyot sunulmaktadır. Cihaz kapasitif fotokurulum üretmekte ve daha yüksek V_{OC} sayesinde tandem olmayan yapılarına kıyasla daha yüksek iyonik yük enjekte etmektedir.

Geliştirilen biyolojik ara yüzler, çeşitli test koşullarında düşük *in vitro* toksisite ve kararlı fotoelektrik performans göstermektedir. Bu sonuçlar, söz konusu kuantum nokta tabanlı tandem fotodiyotun, retinal uyarım için yüksek çözünürlüklü, verimli ve güvenli bir platform olarak potansiyelini ortaya koymakta; aynı zamanda esnek ve ölçeklenebilir bioelektronik ara yüz çözümleri sunmaktadır.

ACKNOWLEDGMENTS

I would like to express my thanks to my advisor, Prof. Sedat Nizamoğlu for his tremendous support through my MSc study.

I would like to thank my thesis committee: Prof. Sennaroğlu and Prof. Çelik for their helpful suggestions and valuable time.

In addition, I expresses gratitude to the Koç University Surface Science and Technology Center (KUYTAM). I gratefully acknowledge the utilization of services and resources provided by the Koç University Research Center for Translational Medicine (KUTTAM), which is funded by the Republic of Turkey Ministry of Development.

The project is funded by Scientific and Technological Research Council of Turkey (TUBITAK) with Project No 121E376 and the European Union (ERC, MESHOPTO, 101045289).

I am very lucky to meet all the current and former IDEALAB members, specially Uğur Berkay Çalışkan and Eren Tekinay.

I would like to thank all my family members for their support through all my education.

I would like to extend my heartfelt gratitude to my friends for their support and companionship. Their presence and friendship have been invaluable throughout this journey.

Finally, my deepest gratitude belongs to my fiancée, Parmida, whose unwavering love and support were the constant strength that made this achievement possible.

TABLE OF CONTENTS

LIST OF TABLES

LIST OF FIGURES

ABBREVIATIONS

NIR	Near-Infrared
QD	Quantum Dot
PV	Photovoltaic
PC	Photocurrent
V_{OC}	Open-Circuit Voltage
J_{SC}	Short-Circuit Current Density
ICL	Interconnection Layer
aCSF	Artificial cerebrospinal fluid
PLL	Poly-L-Lsysine
CTG	CellTiter-Glo
SEM	Scanning electron microscopy
ITO	Indium tin oxide
ETL	Electron transfer layer
HTL	Hole transfer layers
NC	Nanocrystal
TMAI	Tetramethylammonium iodide
ZnO	Zinc oxide
P3HT	poly(3-hexylthiophene)
PEDOT:PSSpoly	(3,4-ethylenedioxythiophene):poly(styrenesulfonate)
RuO_2	Ruthenium oxide
WE	Working electrode
RE	Reference electrode
CE	Counter electrode
TEM	Transmission electron microscopy
XRD	X-ray Diffraction

Chapter 1

INTRODUCTION

Neurostimulation systems are critical therapeutic tools used globally to manage a variety of neurological and physiological disorders, including Parkinson's disease [3], epilepsy [4], heart failure [5], and hearing loss [6]. While traditional wired systems offer proven efficacy, they necessitate invasive surgical procedures, leading to long-term maintenance challenges and mechanical mismatch with soft tissue [7]. Consequently, wireless, minimally invasive optoelectronic interfaces have emerged as a highly promising alternative [8–10]. Light-based neurostimulation offers precise spatial and temporal control, with the utilization of Near-Infrared (NIR) light being particularly advantageous for deep-tissue implantation as it minimizes scattering and penetration depth, thereby eliminating the need for rigid optical fibers [11].

The realization of flexible, high-performance optoelectronic biointerfaces is critically constrained by material limitations. Traditional rigid silicon-based devices demonstrated early success [12], but silicon's low NIR absorption demands thick, inflexible layers. This necessitates the use of thin, solution-processable photoabsorber materials with high NIR absorption coefficients, such as colloidal quantum dots (QDs). While QDs offer desirable optical stability, the most efficient NIR-absorbing candidates (e.g., PbS [1] and HgTe [13]) suffer from severe biocompatibility and toxicity concerns due to the potential for unwanted pH change of the cellular environment [14] or release of heavy metal ions [15]. Safer alternatives typically lack sufficient NIR absorption[16–18]. To overcome this, we select $AgBiS_2$ nanocrystals (NCs) [2] as the foundational photoabsorber due to their heavy-metal-free composition, robust NIR absorption (approaching 10^5 cm^{-1}), and solution processability.

Despite resolving the material toxicity and flexibility challenges with $AgBiS_2$, a

key architectural problem persists. To achieve high spatial resolution in devices, Photovoltaic (PV) pixels must be miniaturized, which drastically lowers the total charge injection capacity. Single-junction PV devices with small pixels cannot reliably provide the open-circuit voltage (V_{OC}) necessary for safe and effective neural stimulation under low, safe illumination levels[19].

The core innovation of this thesis is the strategic translation of the tandem device architecture from high-efficiency solar cells to solve this bioelectronic challenge of insufficient charge injection. By designing the first reported homo-tandem photovoltaic biointerface based entirely on $AgBiS_2$ NCs, we are able to significantly increase the output voltage (V_{OC}) compared to a single-junction device. This voltage increase is critical because it enhances the total charge injection capacity, thereby enabling improved stimulation performance.

The primary objectives of this research are threefold: (1) to design, fabricate, and characterize $AgBiS_2$ homo-tandem photodiode; (2) to determine the enhanced voltage output and charge injection capability of the homo-tandem device using photo-electrochemical tests; and (3) to validate the effectiveness of the $AgBiS_2$ homo-tandem device for neurostimulation using electrophysiology tests. The successful demonstration of this architecture provides a robust, non-toxic, and high-efficiency platform, accelerating the development of next-generation, fully wireless neurostimulation technologies.

The remainder of this thesis is organized as follows. Chapter 2 provides the background and literature review, introducing wireless neurostimulation, optoelectronic biointerfaces, and the fundamental principles of tandem device engineering. Chapter 3 describes the device architecture and material properties, including the role of charge transport layers and characterization of $AgBiS_2$ nanocrystals. Chapter 4 discusses the key design challenges encountered in developing the tandem photodiode, with a focus on interconnecting layer selection, current matching, and low-temperature processing strategies. Chapter 5 presents the optoelectronic and biointerface evaluation of the fabricated devices, comparing the single-junction and tandem configurations through photovoltaic, photoelectrochemical, and patch-clamp measurements, as well as biocompatibility assays. The experimental procedures and

fabrication steps are summarized in Chapter 6. Finally, Chapter 7 concludes the thesis with a summary of the main findings and highlights future directions for advancing flexible tandem photodiodes in neural stimulation applications.

Chapter 2

BACKGROUND

The beginnings of bioelectricity date back as far as Egypt, Greece, and Rome, where electric discharges from eels, catfish, and torpedo rays were employed therapeutically for the relief of pain and for promoting blood circulation. In Egyptian medicine, electric catfish were said to be applied to patients who suffered from arthritis or headaches, while the Roman physician Scribonius Largus described treatment of gout and neuralgia using the torpedo ray. Scientific appreciation for the phenomena of bioelectricity, however, would not occur until the late 18th century with the discovery of 'animal electricity' by Luigi Galvani, who demonstrated that electrical discharges applied to frog legs could generate muscle contractions. Advances in theoretical science evolved during the 19th century, starting with the discovery of the action potential and seminal electrophysiological research by Hermann von Helmholtz and Emil du Bois-Reymond. Another major step was taken in 1952 with the Hodgkin–Huxley model, when it was quantitatively explained how nerve impulses propagate, based on ion mechanisms. The development of the patch-clamp technique by Erwin Neher and Bert Sakmann in the 1970s further revolutionized electrophysiology, providing the capability for directly measuring single-ion channel activity and establishing a methodology that has yet to become obsolete.

Building on these foundations, electrical neurostimulation has emerged as an essential tool in neuroscience research and for medical therapy. Neurostimulation through controlled electrical pulses can either excite or inhibit neural activity by the modulation of neuronal membrane potentials, thereby offering a non-pharmacological method for the restoration or regulation of physiological function. Modern bioelectronic devices, such as cardiac pacemakers, cochlear implants, deep brain stimulators, and vagus nerve stimulators, have already shown clinical efficacies in heart failure, hearing loss, epilepsy, diabetes, and even Parkinson's disease.

The continuous incorporation of knowledge in bioelectricity into material science, microelectronics, and computational modeling transformed neurostimulation from a physiological curiosity into the mainstay of modern biomedical engineering, bridging centuries of discovery from ancient electrotherapy up to state-of-the-art neural interfaces.

2.1 Wireless Neurostimulation and Optoelectronic Interfaces

Neural stimulation plays a crucial role in understanding complex neural circuitry and its correlation with specific behaviors, as well as in therapeutic interventions for neurological disorders [20, 21]. Its underlying mechanism involves the application of controlled electrical currents that modulate ion fluxes, primarily sodium (Na^+) and potassium (K^+), across neuronal membranes due to potential differences between active and return electrode[22]. Whereas direct electrical stimulation through implanted leads remains the most established and effective means, it entails a number of challenges, not least the invasiveness associated with surgical implantation and the very limited selectivity in neural circuit targeting or modulation. Such limitations have encouraged wireless and less invasive stimulation strategies to achieve finer neural control while reducing clinical burden.[23]

In recent years optoelectronics neural interfaces have emerged as a promising alternative, leveraging light to modulate neuronal activity with enhanced spatiotemporal precision and reduced invasiveness compared to traditional electrical methods[24, 25]. This approach uses photodiode-based systems, where incoming photons generate electron-hole pairs in semiconductor materials. These charges are then separated by internal electric fields, producing a localized electrical potential that can interact with nearby nerve cell membranes[26, 27]. Unlike conventional electrical devices, these systems leverage the precision and adaptability of light to selectively activate or inhibit specific neurons. By using different wavelengths, they enable complex stimulation patterns and the targeting of distinct neurons. This process allows for highly targeted neural activation, which is particularly useful in medical treatments requiring precise control of specific groups of neurons[28–30].

These platforms provide a less invasive way to access deep brain regions, potentially replacing or enhancing current deep brain stimulation (DBS) methods[31–33]. Another example of this approach is the use of silicon-based photovoltaic arrays to help restore vision in people with macular degeneration[34–38]. These stiff devices can stimulate the remaining retinal neurons, leading to partial vision recovery. However, their rigidity poses challenges for long-term integration with soft tissue and may cause compatibility issues over time. To overcome this, researchers are now focusing on developing flexible optoelectronic devices that better match the structure of neural tissue, reducing mechanical stress and minimizing long-term inflammation[39].

The inherent flexibility of these next-generation interfaces allows for improved conformability with biological tissues, thereby enhancing the stability and efficacy of chronic neural stimulation[40–43]. However, designing and building these systems comes with significant challenges. Key among them is selecting photoactive materials with the right energy band structure to efficiently generate and move charge carriers[44–47]. It's also crucial to maximize light absorption in ultra-thin devices, often just a few micrometers thick, so they remain flexible while still being sensitive to light[1].

To effectively stimulate neurons, these materials must also deliver enough charge. Traditional methods that rely on capacitive charge delivery can fall short, as they often only provide brief bursts of stimulation[48]. As a result, scientists are exploring materials like PEDOT:PSS, titanium nitride (TiN), and ruthenium oxide (RuO_2), which have better charge storage capabilities and can support stronger stimulation[1, 49, 50]. Even so, these materials might not fully meet the demands of consistent, reliable neural activation, underscoring the need for continued innovation in both materials and device design.

A promising approach to enhance charge injection is to use tandem structures. These structures offer increased generated voltage and charge injection levels[19].

2.2 Tandem Architectures for Enhanced Photovoltage and Charge Injection

The efficiency of a single-junction photovoltaic device is limited by the necessity to compromise between absorbing high-energy photons, minimizing thermalization losses, and collecting lower-energy photons. This compromise leads to the well-known Shockley–Queisser (SQ) limit of approximately 33% under AM1.5G illumination[51]. Tandem photovoltaic devices seek to overcome this ceiling by stacking multiple photoactive layers with distinct or, in some cases, identical bandgaps[52]. In hetero-tandem designs, the subcells have different bandgaps and are spectrally complementary[53–56]. However, an important class of devices, homo-tandems, uses the same bandgap in both subcells yet still achieves substantially higher efficiency than the corresponding single-junction cell [57–59]. his improvement arises not from spectral splitting but from electrical advantages and improved recombination management. Quantum dots offer additional design freedom across both hetero- and homo-tandem configurations. Their bandgap tunability through size and composition, strong absorption coefficients, and ability to passivate interfaces make them attractive for designing either top or bottom subcells.

A key benefit of tandem photovoltaics lies in the boosted V_{OC}, which roughly equals the sum of the voltages from individual subcells in a series-connected setup. Consequently, even homo-tandems, where both subcells have identical bandgaps, can deliver a total V_{OC} that surpasses a single-junction device by hundreds of millivolts. This gain arises as each subcell generates its own quasi-Fermi level splitting independently; substituting a thick absorber with two thinner, well-passivated layers enhances radiative efficiency and curtails recombination losses in each, yielding greater overall photovoltage[60]. This elevated voltage holds significant promise for bio-optoelectronic and biointerface systems, especially those employing photovoltaic charge injection to activate biological tissues[19]. For instance, neural or cardiac photostimulation devices typically demand capacitive or faradaic charge production at electrode-electrolyte interfaces, where the maximum safe and effective charge delivery hinges on the photovoltaic source's available driving voltage.

High-performance tandem photovoltaic cells require three key design principles: well-aligned band offsets, highly efficient interlayers, and current matching between adjacent subcells[61, 62]

In heterojunction tandem solar cells, subcells with complementary bandgaps are selected to enable efficient spectral partitioning[53–56]. Optimal two-junction tandems generally combine a top cell with a bandgap of ∼1.7–1.8 eV and a bottom cell of ∼1.0–1.1 eV[52]. Perovskite/silicon tandems feature a fixed bottom-cell bandgap of ∼1.1 eV (silicon)[56], whereas all-perovskite tandems require tuning of both bandgaps via halide composition or Pb–Sn alloying[55]. Quantum dots enhance design flexibility by enabling bottom cells with tunable bandgaps extending into the deep infrared[54], as well as hybrid perovskite–quantum dot absorbers that exhibit greater stability and lower defect densities.

In homo-tandem configurations, identical bandgaps are employed in both subcells; however, splitting photogeneration across two thinner layers mitigates bulk and Shockley–Read–Hall recombination, thereby increasing the quasi-Fermi level splitting in each subcell[57–59]. The cumulative result is elevated V_{OC} (e.g., > 1.8 V in polymer homo-tandems[59]) and, frequently, superior fill factors. Quantum dots amplify these benefits via targeted passivation and interface optimization, which suppress non-radiative losses relative to single-junction cells of equivalent thickness[57].

The interconnection layer constitutes a critical element in monolithic tandem solar cells, as it must enable efficient charge recombination, ensure optical transparency, suppress parasitic absorption, and endure subsequent fabrication processes. An optimal ICL establishes an ohmic recombination junction free from voltage losses, optical attenuation, or chemical incompatibilities with adjacent subcells[63, 64]. Conventional III–V tandems have employed epitaxial tunnel junctions[65]; however, solution-processed tandems demand more adaptable materials, including transparent conductive oxides, metal oxides, organic charge-transport layers, and hybrid multilayers[63, 66, 67]. Recent developments have emphasized the advantages of incorporating ultrathin metallic films , such as sub-10 nm layers of Au, Ag, or Cu,war within the ICL stack. When appropriately engineered, these films deliver high lateral conductivity and uniform morphology while maintaining semitransparency. They

further promote effective carrier recombination via intermediate energy states or enhanced tunneling across neighboring transport layers. In addition, such thin metals function as protective barriers, safeguarding sensitive perovskite or quantum dot layers from plasma damage during transparent conductive oxide sputtering[66].

The last essential principle and a primary challenge in realizing high-performance two-terminal monolithic tandem solar cells is current matching between the subcells[61]. In this series-connected architecture, the overall photocurrent is constrained by the subcell generating the lowest current, which in turn limits the device's efficiency. A standard approach to resolve this is to adjust absorber layer thicknesses such that both subcells yield equivalent currents. Optical modeling is particularly effective for this purpose, as it predicts subcell photocurrents across various thicknesses to inform tandem structural optimization[68]. Complementary techniques, including modified detailed-balance analyses[69]and semi-empirical models[70], have similarly guided thickness optimization to attain balanced currents.

2.3 Motivation and Objectives of the Study

The motivation behind this research project arises from the need to advance the performance of flexible optoelectronic neural interfaces by overcoming the inherent limitations in charge injection efficiency found in current photostimulation platforms. While optoelectronic neural interfaces offer exciting prospects for minimally invasive, wireless stimulation, their effectiveness is fundamentally constrained by the modest photovoltage and charge density generated by conventional single-junction photodiodes. These limitations restrict both stimulation strength and long-term biocompatibility. Therefore, this project aims to address these challenges by introducing a tandem photodiode architecture that enhances photovoltage, improves charge injection levels, and maintains compatibility with neural tissue.

The main focus is to explore the potential of integrating a tandem photodiode structure into a flexible optoelectronic biointerface to achieve high-efficiency photostimulation under low-intensity illumination. Several objectives guide this study. First, the goal is to fabricate a flexible tandem photodiode using a straightforward,

reproducible manufacturing route compatible with biointerface requirements. Next, the photovoltage, photocurrent, and photogenerated charge density of the tandem architecture will be characterized in biological media. Special emphasis will be placed on evaluating how the increased open-circuit voltage (V_{OC}), a core advantage of tandem structures, translates into improved capacitive charge injection. The biocompatibility of the full device stack will be assessed, followed by patch-clamp electrophysiology on hippocampal neurons to examine their response to photostimulation driven by the tandem photodiode. Finally, the overall performance of the interface will be evaluated to determine its ability to elicit stable and repetitive neuronal firing.

This study contributes to the field by demonstrating, for the first time, the use of a flexible tandem photodiode specifically engineered for neural photostimulation. By leveraging the increased photovoltage and reduced recombination losses inherent to tandem architectures, this work aims to significantly elevate charge injection levels beyond what is achievable with single-junction devices. The study's novelty lies in applying tandem optoelectronic structures, traditionally used for photovoltaics, to biointerfaces, thus bridging two fields to unlock higher stimulation efficiency without compromising biocompatibility.

The findings from this research will provide new insights into the role of multilayer photodiodes in bioelectronic systems, highlight the potential of tandem device engineering for neural stimulation applications, and expand the design space for next-generation optoelectronic neural interfaces. Ultimately, this project aims to contribute to the advancement of bioelectronic medicine by enabling safer, stronger, and more energy-efficient neural stimulation modalities for future therapeutic applications.

Chapter 3

DEVICE ARCHITECTURE AND MATERIAL PROPERTIES

3.1 Fundamentals of Quantum Dot Photovoltaics

Quantum dots are semiconductor nanocrystals whose optoelectronic properties are governed by quantum mechanical effects, enabling tunable bandgaps based on size and composition[71]. This quantum confinement effect allows for precise engineering of light absorption and emission characteristics, making them highly suitable for various photovoltaic applications[1]. Moreover, the ability to control the bandgap via material size enables the modification of the absorption spectrum and extinction coefficient[72].

Despite these advantageous properties, the efficiency of quantum dot solar cells remains suboptimal due to challenges such as lower charge carrier concentrations and mobility[73]. To enhance performance, various strategies are being explored, including the optimization of quantum dot materials, interface engineering, and novel device architectures, often focusing on non-toxic alternatives to traditional lead, cadmium, and mercury-containing QDs[44]. The integration of $AgBiS_2$ quantum dots within a photostructure typically involves an electron transport layer like ZnO, which is inherently n-type, and a hole transport layer such as poly(3-hexylthiophene)(P3HT), to facilitate efficient charge separation and transport[1, 26].

This tripartite structure optimizes carrier extraction, where the electron transport layer and hole transport layer collectively contribute to the internal electric field, thereby improving current generation and overall device efficiency[74]. A well-designed heterostructure involving these layers can suppress electron-hole recombination and improve charge mobility, further boosting the efficiency of the quantum dot solar cells[75]. The judicious selection and engineering of the electron transport

layer and hole transport layer are critical for maximizing power conversion efficiency and long-term device stability[76, 77]. This includes optimizing the band alignment between layers and ensuring efficient charge transfer at the interfaces.

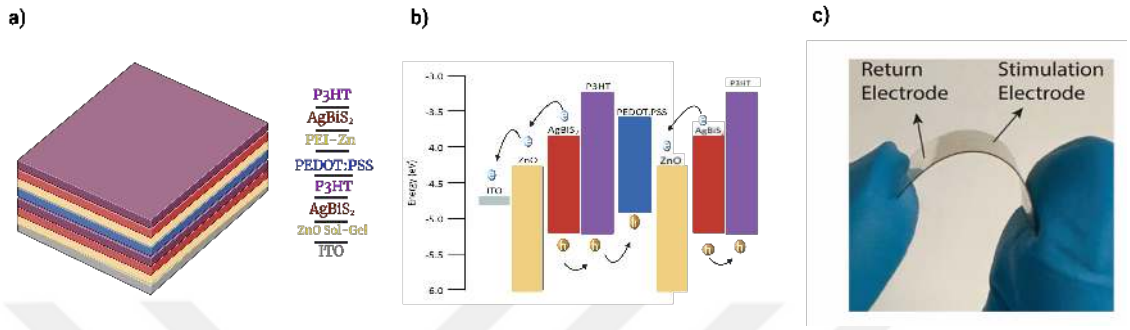

Figure 3.1: a) Schematic of the biointerface (not to scale). b) Energy band diagram of the photodiode. c) Photograph of the flexible biointerface on PET/ITO substrate.[1]

3.2 Role of Charge Transport Layers

The electron transport layer typically comprises a material with high electron mobility and appropriate energy alignment to accept electrons from the quantum dots while blocking holes, a function often fulfilled by zinc oxide due to its high electron mobility and suitable band alignment[47]. Conversely, the hole transport layer, such as P3HT, is engineered to selectively extract holes from the quantum dot active layer and transfer them to the anode, simultaneously preventing electron recombination at the interface and enhancing carrier selectivity[78]. This intricate interplay of materials and their energetic landscape dictates the overall efficiency and stability of the quantum dot solar cell[79]. The interface between these layers also plays a critical role, as surface states can mediate charge exchange, potentially leading to photoelectrochemical processes and reduced performance[47]. Therefore, careful engineering of these interfaces is essential to mitigate surface recombination and optimize charge transfer kinetics, directly impacting the device's power conversion efficiency[26].

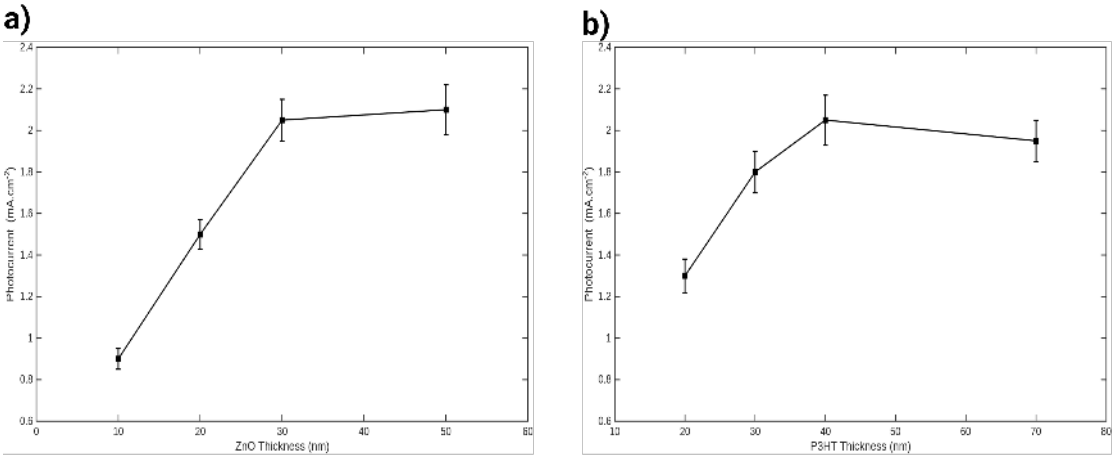

Figure 3.2: Photocurrent measurements for different a) ZnO and b) P3HT layer thickness under NIR light illumination (mean ± SEM, n=5).[2]

3.2.1 Impact of ZnO ETL on Device Performance

The electron extraction properties of the zinc oxide ETL are paramount for maximizing the performance of quantum dot photodiode, primarily by facilitating rapid electron transport while simultaneously blocking hole migration towards the anode. This function is critically dependent on the ZnO's band alignment with the quantum dot layer, ensuring a favorable energy cascade for electrons (Figure 3.1b).

The morphology and conductivity of the ZnO layer significantly influence charge extraction efficiency, with denser, more uniform films typically leading to improved performance[40]. The deposition conditions of ZnO, such as annealing temperature, and oxygen pressure, significantly influence its optical and electrical properties, directly impacting its effectiveness as an ETL[80]. Optimizing these parameters can lead to a reduction in defects and an improvement in the crystallinity of the ZnO layer, which, in turn, enhances electron mobility and eliminates potential recombination pathways[40].

The thickness of the ZnO thin film is a critical parameter influencing the performance of quantum dot solar cells, as it directly impacts charge transport kinetics, optical transparency, and the overall resistance of the device. Optimal thickness ensures efficient electron extraction while minimizing series resistance and maximizing

light transmission to the active layer. An excessively thick ZnO layer can impede charge collection due to increased resistance and light absorption, while an overly thin layer may lead to incomplete coverage and inefficient electron extraction, thus highlighting the need for precise thickness optimization. Accordingly, as shown in Figure 3.1a, the ZnO ETL thickness was systematically optimized to achieve a balance between efficient electron extraction, low series resistance, and high optical transparency, leading to improved overall device performance.

3.2.2 Impact of P3HT HTL on Device Performance

The integration of $AgBiS_2$ QDs with P3HT within a bulk heterojunction structure also leverages the advantages of organic semiconductors, such as flexibility and low-cost processing, while simultaneously improving charge separation and transport[35]. The P3HT hole transport layer plays a crucial role in preventing charge recombination at the $AgBiS_2$/electrode interface and facilitating efficient hole extraction due to its favorable energy levels and high hole mobility, significantly enhancing overall device performance. Moreover, the judicious selection of P3HT, or similar hole transport materials, is essential for optimizing the interface energetics and minimizing energetic barriers for hole transfer from the $AgBiS_2$ quantum dots. The specific band alignment of P3HT with $AgBiS_2$ is crucial for ensuring efficient charge separation and preventing recombination losses, thereby maximizing the power conversion efficiency of the photovoltaic device[46].

The excellent film-forming properties and solution processability of P3HT also contribute to its utility in scalable fabrication methods for high-performance devices[1]. Furthermore, P3HT's established biocompatibility and biodegradability make it particularly well-suited for implantable bioelectronic devices, including retinal prostheses, where long-term stability and minimal tissue response are critical considerations[35]. The high biocompatibility of P3HT also contributes to the reliable bionanojunctions in biointerfaces, potentially reducing the need for additional interfacial layers to enhance cell adhesion[44].

As with the ZnO electron transport layer, the thickness of the P3HT hole trans-

port layer is a crucial factor for quantum dot solar cells because it affects charge transport kinetics, optical losses, and, hence, the total series resistance of the device. Optimal P3HT thickness allows efficient hole extraction at minimal resistive losses and parasitic absorption. Indeed, too thick a layer of P3HT would impede the charge transport due to increased series resistance, while a too thin layer would result in poor coverage and inefficient hole extraction. For these reasons, the P3HT thickness was systematically optimized following the same considerations and optimization strategy applied to the ZnO layer. As a result, Figure 3.1b shows that such an optimization allowed balancing efficient hole extraction, low series resistance, and less optical losses toward an improved general device performance.

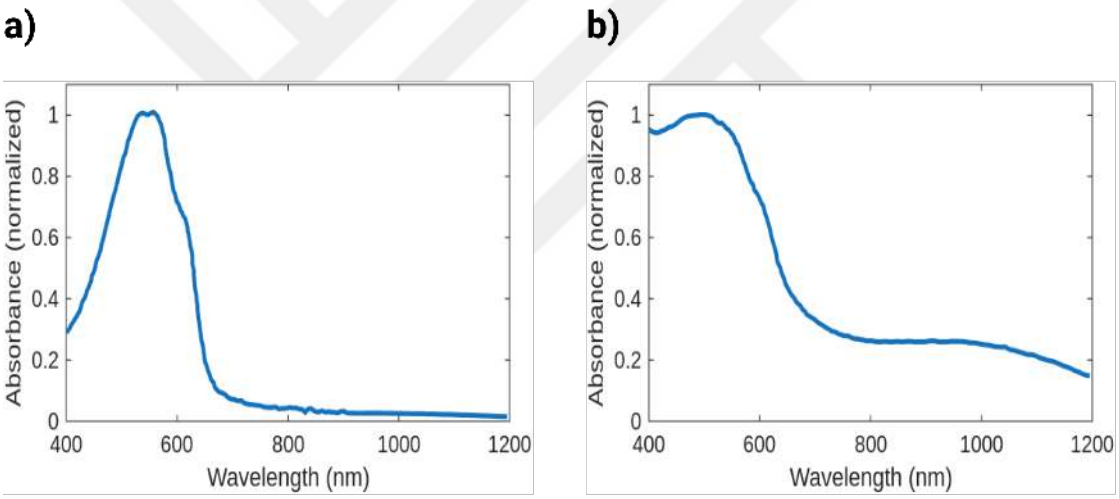

Figure 3.3: Absorbance spectra of a) ITO/ZnO/P3HT and b) ITO/ZnO/$AgBiS_2$/P3HT, showing that the absorbance in the NIR range originates from the $AgBiS_2$ nanocrystal layer.[2]

3.3 Role of Photoabsorber Layer

The $AgBiS_2$ quantum dot layer serves as the primary light-absorbing component, converting incident photons into electron-hole pairs, which is a critical determinant of the solar cell's efficiency and spectral response. The exceptional tunability of its bandgap, through precise control over quantum dot size and composition, allows for

optimized light harvesting across a broad spectrum, particularly in the near-infrared region[81].

These optical properties make the material particularly suitable for biointerface applications aimed at neural stimulation using near-infrared (NIR) light. As shown in the absorbance spectrum in Figure 3.3a, the device exhibits pronounced absorption in the NIR region, which is essential for efficient light harvesting at wavelengths that offer deeper tissue penetration and reduced phototoxicity. This NIR responsiveness enables effective photogeneration of charge under biologically relevant illumination conditions, thereby supporting its applicability as an optoelectronic biointerface for neurostimulation. The absorbance spectrum of ZnO and P3HT indicates negligible absorption in the near-infrared (NIR) region, confirming that the device operation under NIR illumination arises exclusively from the contribution of the $AgBiS_2$ nanocrystal layer (Figure 3.2).

Moreover, the ability of quantum dots to be processed from solution offers a cost-effective and scalable manufacturing route for various optoelectronic devices[82].

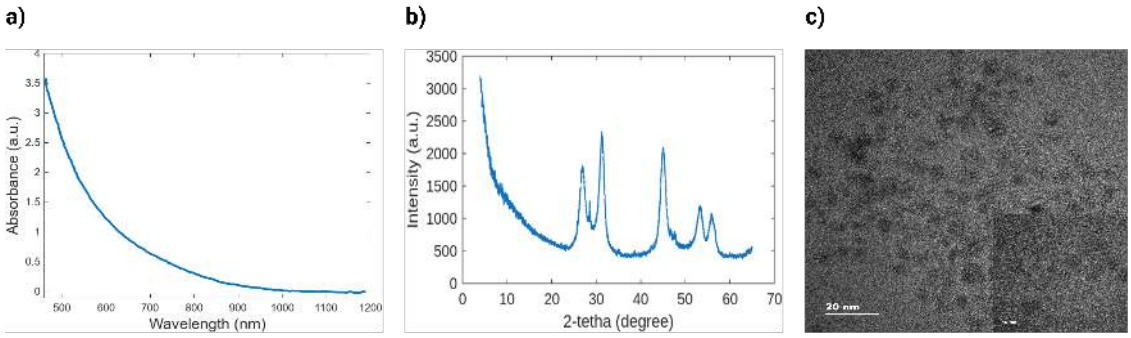

Figure 3.4: a) Absorbance of $AgBiS_2$ NCs.[2] b) The X-Ray diffraction (XRD) spectrum of $AgBiS_2$ NCs. c) Transmission electron microscopy (TEM) image of $AgBiS_2$ NCs.

3.4 Characterization of $AgBiS_2$ Layers

Given the critical role of $AgBiS_2$ as the light-absorbing quantum dot layer, comprehensive characterization of its structural, optical, and electrical properties is

indispensable for understanding device performance. This characterization often involves techniques like transmission electron microscopy to visualize the quantum dot morphology and confirm successful integration into the device architecture (Figure 3.3c). Additionally, X-ray diffraction can confirm the crystalline structure and phase purity of the $AgBiS_2$ quantum dots, which directly impacts their electronic band structure and charge transport capabilities (Figure 3.3b). Optical characterization, including UV-Vis absorption and photoluminescence spectroscopy, further elucidate the electronic transitions and emission properties of $AgBiS_2$, providing insights into their light-harvesting efficiency and potential for radiative recombination (Figure 3.3a). Such detailed analyses are crucial for correlating material properties with device performance, guiding further optimization towards higher power conversion efficiency.

Chapter 4

DESIGN CHALLENGES IN TANDEM PHOTODIODE DEVICES

4.1 Low-Temperature Electron Transport Layer

One of the primary design challenges in monolithic tandem photodiode devices arises from the use of sol–gel–processed ZnO as the electron transport layer (ETL). While sol–gel ZnO provides excellent electron extraction and optical transparency; it typically requires high annealing temperatures to achieve sufficient crystallinity and conductivity. Such high-temperature processing is incompatible with tandem architectures, as it can degrade the quantum dot (QD) active layer and organic polymer layers of the second subcell.

To address this limitation, two low-temperature alternatives to sol–gel ZnO were investigated: ZnO nanoparticles (ZnO NPs)[83] and polyethyleneimine-modified ZnO (PEI–Zn)[84]. These materials can be processed at significantly lower temperatures, making them more suitable for tandem integration without compromising the underlying layers.

The photocurrent and photovoltage generated by devices incorporating these alternative ETLs were systematically compared to those obtained using sol–gel ZnO in the first cell. For ZnO NPs, different doping strategies, including sol–gel ZnO and $MgCl_2$ doping, were explored to improve charge extraction and device performance.

The data indicate that ZnO NP-based ETLs exhibit reduced photocurrent and photovoltage, regardless of the doping approach employed. In contrast, the PEI–Zn ETL demonstrates performance comparable to that of the sol–gel ZnO reference, suggesting effective electron extraction and minimal interfacial losses. These results identify PEI–Zn as a promising low-temperature ETL candidate for tandem photodiode architectures, offering compatibility with temperature-sensitive QD and

organic layers while maintaining device performance.

4.2 Interconnecting Layer Selection and Evaluation

The ICL stands at a critical position in the monolithic tandem photodiode device for providing an effective charge recombination path between the two subcells with high optical transparency. Among them, two material classes are considered widely for the implementation of the ICL: conductive polymers and ultrathin metallic films. Three promising ICL configurations were investigated here: PEDOT:PSS, Ag NW/PEDOT:PSS composites, and an ultrathin gold (Au) layer with a nominal thickness of 3 nm.

For each ICL candidate, two important performance parameters were measured: optical transparency and electrical conductivity. Optical characteristics were determined by absorbance and transmittance spectra, which are presented in Figure 4.1. PEDOT:PSS and Ag NW/PEDOT:PSS displayed a little higher optical transmittance within the relevant spectral range compared to the ultrathin Au layer, indicating a marginal optical advantage for polymer-based interlayers.

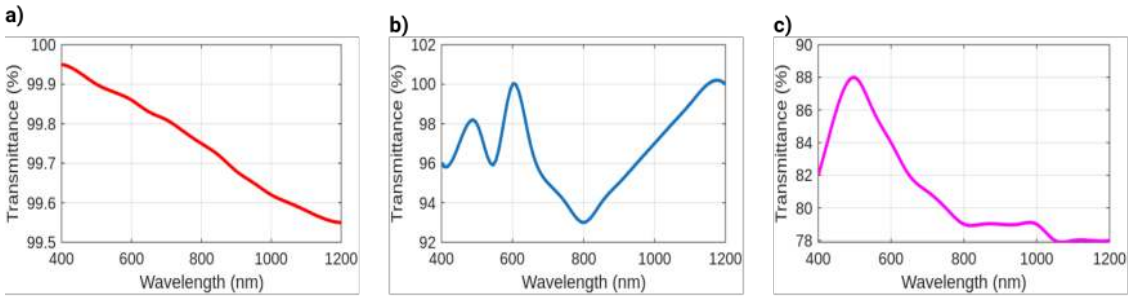

Figure 4.1: Transmittance spectrum of a) PEDOT:PSS. b) Ag nanowire/PEDOT:PSS composite. c) Transmittance of thin Au film.

Electrical performance was characterized by current–voltage (J–V) measurements on test structures with the HTL of the first subcell and the ETL of the second subcell, so that the electrical behavior of the interlayer was isolated[85]. The obtained J–V characteristics are shown in Figure 4.2 and demonstrate a much

lower series resistance for the Au-based ICL compared to the polymer-based ICLs, demonstrating more efficient charge recombination and transport.

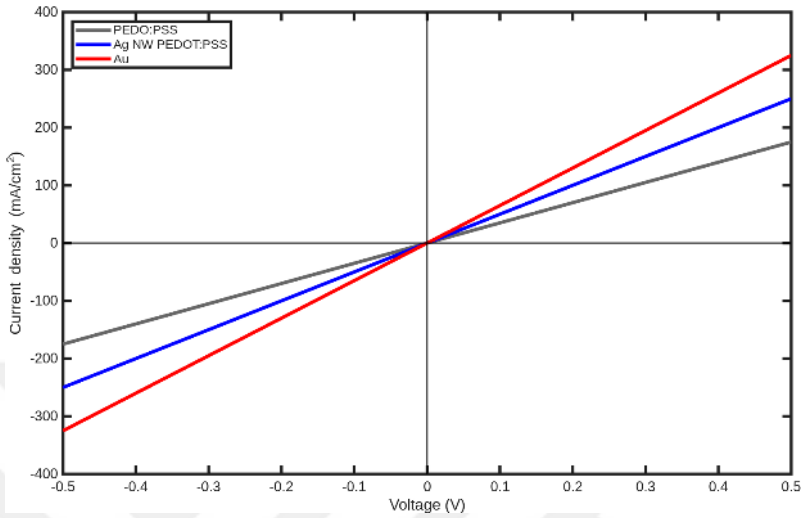

Figure 4.2: Current density–voltage (J–V) characteristics of the candidate interconnection layers.

As such, the ultrathin Au interlayer is selected for subsequent tandem device integration considering both combined optical and electrical results and practical aspects of the fabrication simplicity and process reproducibility. While polymer-based ICLs give a slightly higher optical transmittance, the superior electrical conductivity and ease of fabrication of the Au interlayer will make it more suitable for the tandem photodiode architecture investigated in this study.

Table 4.1: Extracted resistance values for different ICL configurations.

ICL	R_A (Ω·**cm**^{2})	**Transmittance (T%) at 780 nm**
PEDOT:PSS	2.86	99.8%
Ag NW PEDOT:PSS	2.00	93.2%
Au	1.54	79.3%

4.3 Current Matching in Tandem Photodiode Devices

Current matching among subcells is a stringent requisite in the case of a monolithic tandem photodiode architecture, where the overall device performance is limited by the subcell producing the lower photocurrent. Traditional current-matching techniques usually involve careful optimization of the thickness of each photoactive layer through multiple deposition cycles. This approach raises some fabrication complexity and decreases the process reproducibility.

To simplify the process without losing efficient current matching, a different strategy was adopted by tuning the concentration of the $AgBiS_2$ quantum dot ink. Instead of changing the number of deposition cycles, single-cycle depositions were applied for each subcell with $AgBiS_2$ concentrations at 40, 60, 80, and 100 mg mL^{-1}. This allows the systematic modulation of absorber thickness via solution concentration to be achieved with a comparable processing sequence.

In a tandem configuration, the rear subcell suffers from a reduced photon flux due to absorption in the front subcell and therefore usually needs a thicker photoabsorbing layer to compensate for the lower incident light intensity. Devices in a tandem configuration were prepared based on this principle with different combinations of $AgBiS_2$ concentrations in the front and the rear subcells.

The photogenerated voltage and current of these tandem devices were measured by a patch-clamp measurement setup, the results of which are summarized in Figure 4.3. The 60/60 and 60/80 mg mL^{-1} front/rear concentration combinations showed the highest photogenerated current and voltage in the tested configurations, which indicates the effective current matching between the two subcells.

This behavior can be ascribed to a relatively moderate absorption of the front $AgBiS_2$ layer and the correspondingly limited attenuation of incident light reaching the rear subcell. A large disparity in absorber thickness between the front and rear cells is thus not required, and equal concentrations or slightly higher concentration in the rear subcell are sufficient to accomplish current matching by balanced photocurrent generation between the two cells. These results prove that the approach of thickness control based on concentrations provides a practical and scalable route

for current matching in tandem photodiode devices.

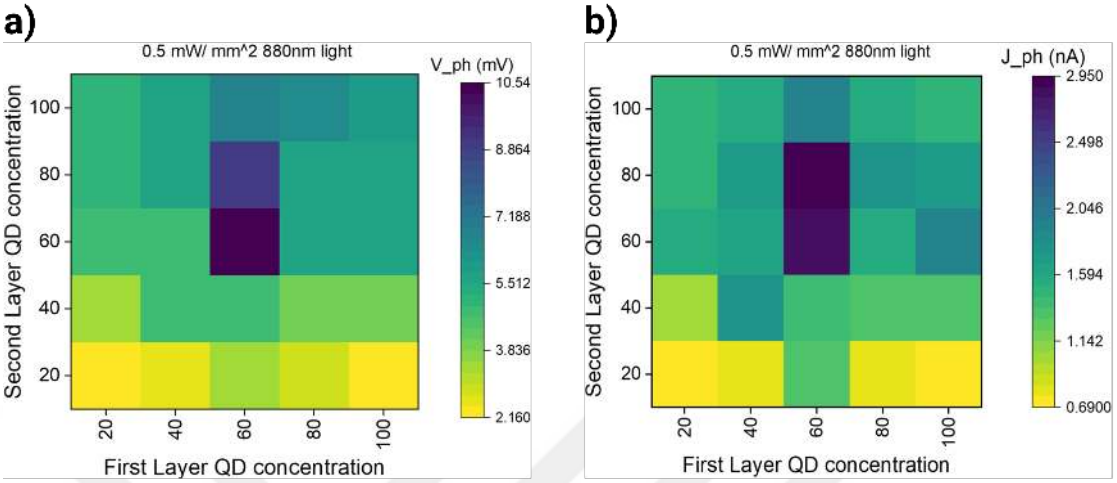

Figure 4.3: Heatmaps showing the dependence of a) photovoltage and b) photocurrent on first and second layer QD concentrations.

Chapter 5

OPTOELECTRONIC PERFORMANCE AND BIOINTERFACE EVALUATION

This chapter describes the optoelectronic characterization and biointerface performance of the fabricated photodiode devices. First, electrical characteristics are measured by standard current–voltage (J–V) and EQE measurements. Then, the photoelectrochemical behavior relevant for biointerface operation is evaluated with standard three-electrode and patch-clamp measurement configurations at biologically relevant light illumination conditions. After that, the performance of tandem devices is compared to single-junction devices in terms of photogenerated current and charge injection.

5.1 Current–Voltage and External Quantum Efficiency Characteristics

The first optoelectronic characterization of the fabricated devices was performed using current–voltage (J–V) and EQE measurements. The J–V characteristics were measured under illumination using a standard solar simulator, thus providing uniform and consistent conditions for reference, when comparing device performance. Resulting J–V curves, along with the corresponding EQE spectra, are presented in Figure 5.1.

Indeed, the tandem configuration presents a substantial increase in photovoltage, which is roughly 60% higher than that in the single-junction device. The voltage improvement points to the successful series connection of the two subcells within the tandem structure. The nonzero voltage gain due to the series connection shows a nonideal 100% voltage increase. These minor losses are related to the voltage drop due to the finite resistivity of the ICL and the current mismatch between the subcells. Obtained key photovoltaic parameters, such as short-circuit current

density and open-circuit voltage from the J–V characteristics are listed in Table5.1.

The EQE spectra further confirm efficient photocarrier generation across the absorption of the active layers and are in good agreement with the trends obtained by the J–V measurements, supporting the observed voltage enhancement in the tandem device.

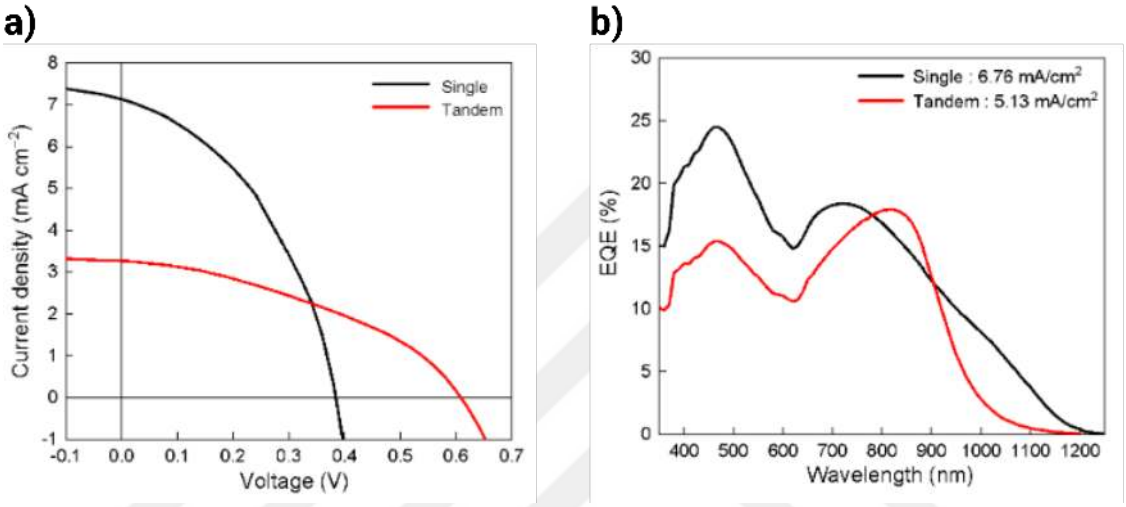

Figure 5.1: Comparison of single-junction and tandem quantum dot photodiodes. a) J–V characteristics under illumination. b) External quantum efficiency (EQE) spectra.

Table 5.1: Photovoltaic performance parameters of the single-junction and tandem devices

Type of Device	V_{oc} (mV)	J_{sc} (mA cm^{-2})	J_{EQE} (mA cm^{-2})
Single	384	7.13	6.76
Tandem	609	3.26	5.13

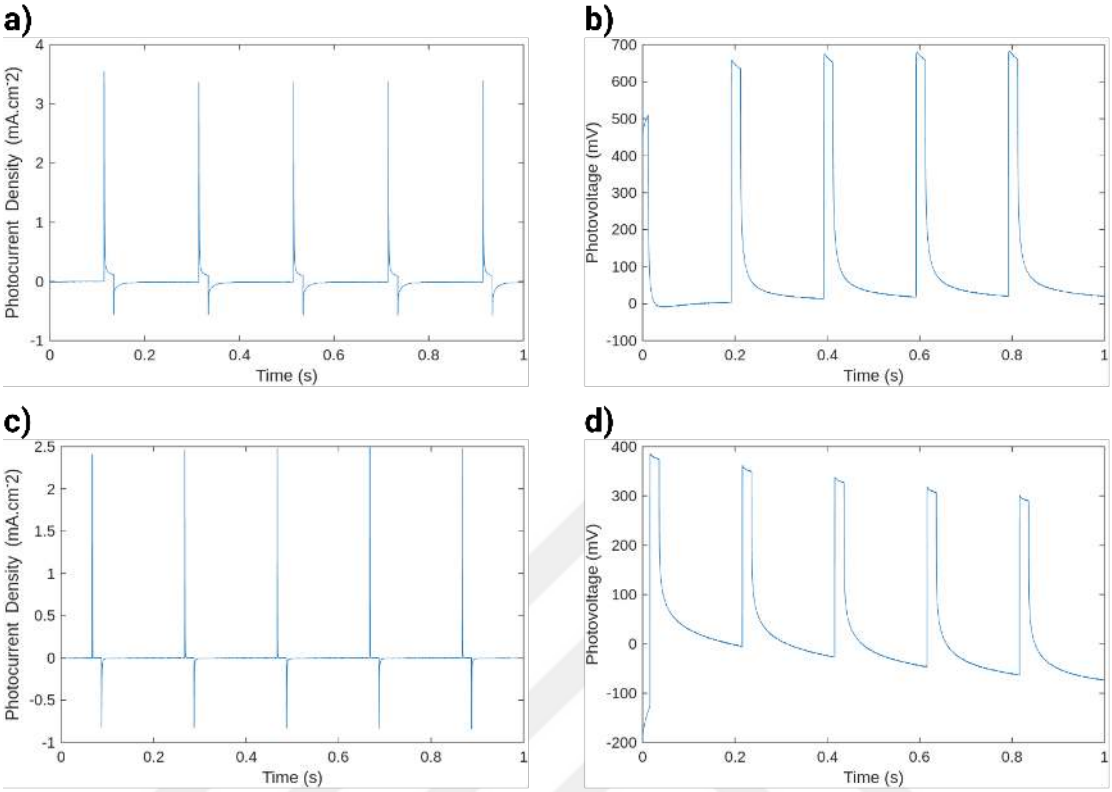

Figure 5.2: Time-resolved a) photovoltage and b) photocurrent density responses of the tandem photodiode. Time-resolved a) photovoltage and b) photocurrent density responses of the single-junction photodiode.

5.2 Photoelectrochemical Characterization

Photoelectrochemical performances of the devices were investigated in a three-electrode configuration setup under near-infrared illumination. A 780 nm light-emitting diode (LED) is used with an intensity of 5 mW cm^{-2} as the excitation source. Illumination was performed in a pulsed mode, with pulse duration of 200 ms and on time of 20 ms to allow for controlled measurement of transient photocurrent and photovoltage response under biologically relevant stimulation conditions.

For both single-junction and tandem photodiode devices, photocurrent and photovoltage responses were recorded. It can be clearly seen from Figure 5.2 that in the case of a tandem device, both PC and PV are enhanced when compared to the single device. The quantitative values obtained from the above measurements are

listed in Table5.2.

Therefore, the enhanced PC and PV of the tandem devices should be attributed to the combined contribution from the two subcells and the effective photovoltage increase, further confirming the advantage of the tandem architecture in applications of optoelectronic biointerfaces in low-intensity and pulsed near-infrared illumination.

Table 5.2: Photovoltaic performance parameters of the single-junction and tandem devices

Type of Device	Photovoltage (mV)	Photocurrent Density (mA cm^{-2})
Single	363	2.45
Tandem	648	3.33

5.3 Patch-Clamp Evaluation

Charge injection capability was directly assessed for the photodiode devices using patch-clamp measurements under conditions relevant to biology. For excitation, an 880 nm laser was applied with varying illumination intensity of 0.5, 1, 2.5, and 5 mW mm^{-2} in a pulsed mode with a pulse duration of 200 ms and an off time of 20 ms. Light was delivered this way to ensure stimulation parameters are precisely controlled and can be compared to the three-electrode measurements.

A variety of light intensities were used to measure photogenerated current and injected charge for both single-junction and tandem photodiode configurations. Figure 5.3 reveals that, for all tested illumination conditions, the tandem devices display superior photocurrent and charge injection compared to the single-junction devices.

This improved performance of the tandem architecture is due to the increased effective photovoltage and more efficient charge separation provided by the series-connected subcells. These results further indicate the advantages of tandem photodiode devices for optoelectronic biointerface applications, especially in cases that require higher charge injection at low-intensity near-infrared illuminations.

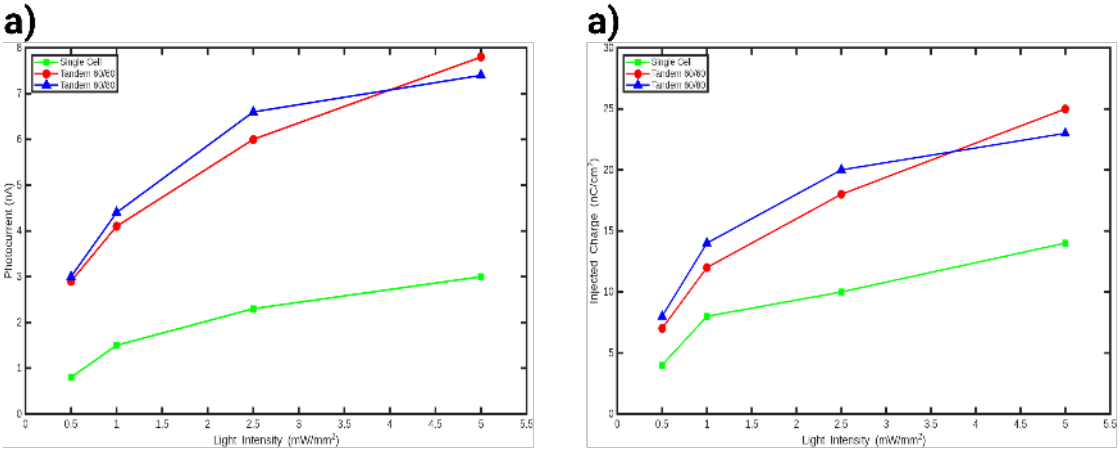

Figure 5.3: a) Photocurrent and b) injected charge as a function of light intensity for single-junction and tandem photodiode architectures.

5.4 Biocompatibility

The neuron characteristics and structural examination of the cytoskeleton in cells cultured on ITO control and tandem devices were performed using double staining of NeuN and f-Actin proteins. In the NeuN staining shown in Figure 5.5a, no difference was observed in the density of NeuN-positive cells, which is the neuron-specific nuclear protein expressed by primary hippocampal cells, between the control ITO and our devices. We have demonstrated the status of cell-to-cell connections by performing actin protein staining. No similar structure was observed in the cell morphology and characteristic features of the primary neurons on the control and our device.

The neuron characteristics and cytoskeleton structure in cells cultured on ITO control and tandem devices were examined using double staining of NeuN and f-Actin proteins. In the NeuN staining shown in Figure 5.5a, no difference was observed in the density of NeuN-positive cells—the neuron-specific nuclear protein of primary hippocampal cells—between the control ITO and our devices. Cell-to-cell connections were evaluated using actin staining. No differences were observed in cell morphology and characteristic features of the primary neurons on the control and our device.

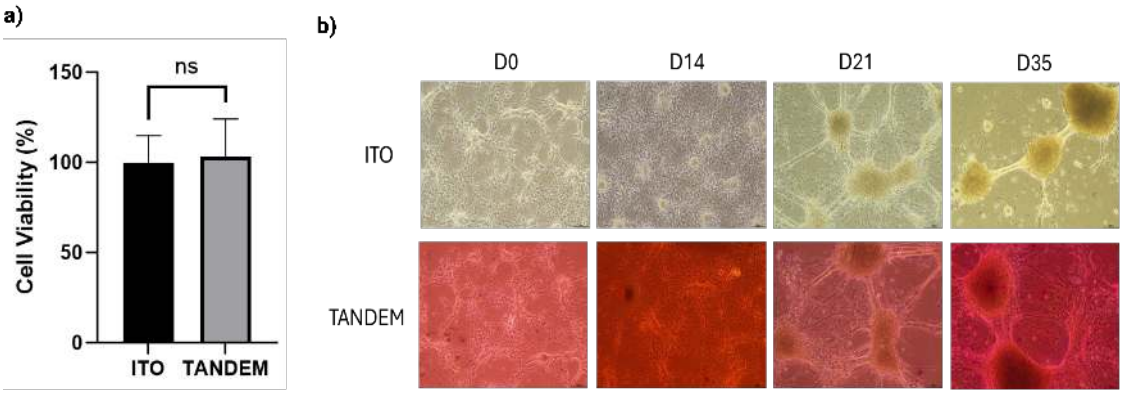

Figure 5.4: a) CTG Biocompatibility of Bio-interfaces. The ITO sample, known to be biocompatible, was used as a control. Significance level was calculated using a two-tailed unpaired t-test; $p < 0.05$ was considered statistically significant. b) Light microscope images of primary hippocampal neurons on Day 0, 14, 21 and 35 following the neuron isolation protocol. The scale bar represents 100 μm.

The cellular death status due to DNA fragmentation in neurons and the examination of the neuron-specific cytoskeleton in cells cultured on ITO control and Tandem devices were performed using TUNEL and beta-III-tubulin double staining. In Figure 5.4b, TUNEL positivity in primary hippocampal cells was detected in a small number of cells on both the control ITO and our Tandem device, and the neuron-specific cytoskeletal protein, beta-III-tubulin, was observed to be similar on both the control ITO and Tandem bio-interfaces.

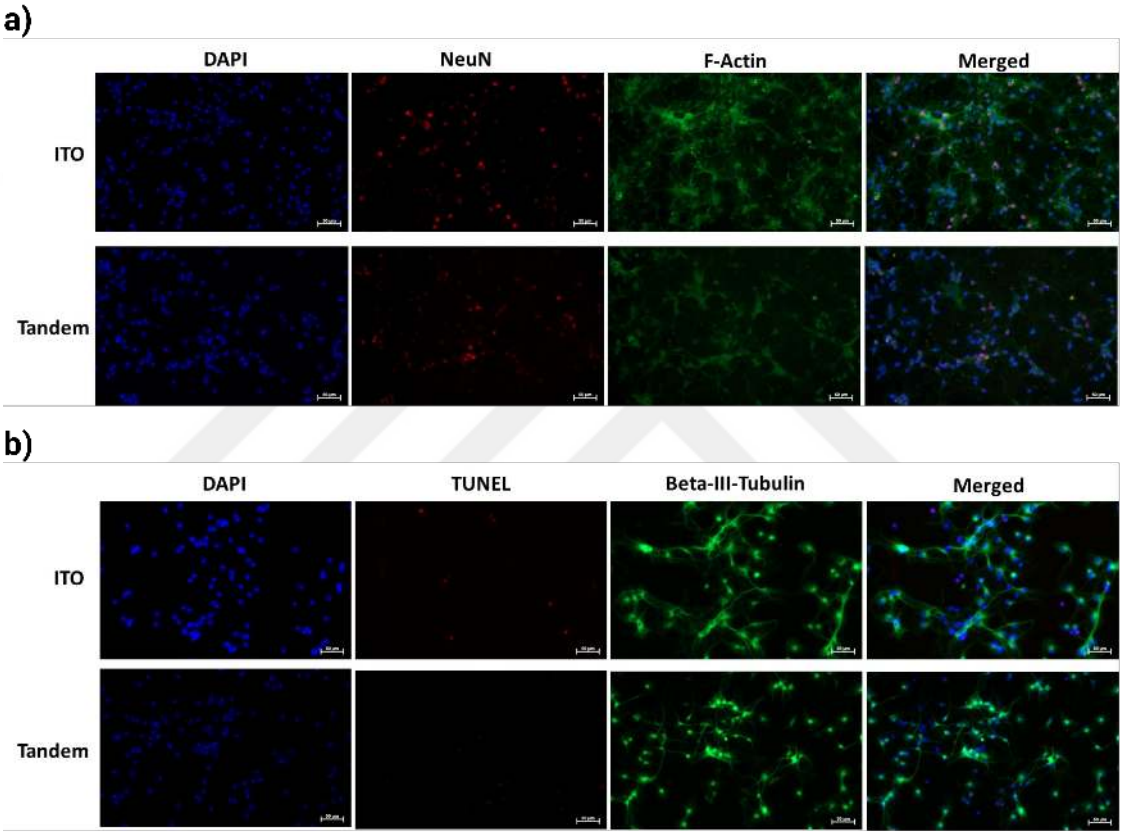

Figure 5.5: Primary hippocampal neurons on ITO control and tandem bio-interfaces stained with TUNEL (red), DAPI (blue), beta-III-tubulin (green), and merged channel images at a) Day 0 and b) Day 14. The scale bar represents 50 μm.

Chapter 6

METHODS

6.1 Biointerface Fabrication

Devices were fabricated on glass/ITO substrates (Ossila, S111). The substrates underwent multiple cleaning steps, starting with sonication in a surfactant solution (HELLMAX II, 3%) mixed with deionized water. This was followed by two rinsing steps: first with pure deionized water and then with a 1:1 (v/v) mixture of ethanol and isopropanol. All steps were carried out for 15 minutes at 50 °C. Finally, to remove any remaining residues, the substrates were treated with UV–ozone for 20 minutes. The ZnO layer was spin-coated on the glass/ITO substrates using a sol–gel method. A precursor solution was prepared by dissolving 220 mg of zinc acetate dihydrate($Zn(CH_3CO_2)_2.2H_2O$, Sigma-Aldrich) and 80 mg ethanolamine ($HOCH_2CH_2NH_2$, Sigma-Aldrich) in 2 mL of 2-methoxyethanol ($CH_3OCH_2CH_2OH$, igma-Aldrich). The solution was sonicated for 30 minutes at 50 °C to obtain a clear and homogeneous mixture. The resulting sol was then spin-coated onto the substrates at 1000 rpm for 60 seconds, followed by annealing at 150 °C for 30 minutes. Next, 50 μL of $AgBiS_2$ solution (60 mg mL^{-1} in toluene) was spin-coated onto the ZnO layer at 1500 rpm for 30 seconds. Subsequently, the film was treated for 60 seconds with a 1% (v/v) solution of tetramethylammonium iodide (TMAI, $(CH_3)_4NI$, Sigma-Aldrich) in methanol, followed by two rinsing cycles using absolute methanol. The film was then annealed at 100 °C for 10 minutes. The P3HT layer was deposited by spin-coating 50 μL of a solution prepared by dissolving 20 mg of P3HT (95.7% regioregular, 99% purity, Ossila) in 1 mL of 1,2-dichlorobenzene. The solution was stirred overnight at 70 °C, and the resulting film was annealed at 150 °C for 15 minutes. An interconnection layer (ICL) made of a 3 nm Au film was then applied by thermal evaporation In a Kurt J. Lesker Nano36 system for tandem devices. The

preparation method for PEI–Znwas adapted from relevant previous work in the literature [84]. To prepare the PEI–Zn precursor solutions, either 0.1 wt.% PEI or 0.5 wt.% PEIE was first dissolved in methoxyethanol, with a small volume of water added to assist solubility. Subsequently, varying amounts of zinc acetate dihydrate or zinc acetylacetonate hydrate was introduced into the PEI or PEIE solution. The mixtures were then stirred continuously for approximately 3 hours prior to the coating step. For the optimized formulation, which corresponds to a Zn-to-N molar ratio of 15:1, 0.075 g of zinc acetate dihydrate was added to 1 mL of the PEI or PEIE solution (including the added water). The solution was stirred until fully transparent, indicating complete dissolution. Notably, the addition of a small amount of water (around 10 μL) played a critical role in promoting the dissolution of the zinc salts in the polymer matrix. The same deposition techniques used for the first cell were then used to fabricate the second cell on top of the PEI–Zn. For flexible biointerfaces, identical fabrication procedures were carried out on PET/ITO substrates.

6.2 Synthesis and Characterization of $AgBiS_2$ QDs

6.2.1 Synthesis of $AgBiS_2$ QDs

Colloidal $AgBiS_2$ quantum dots (QDs) were synthesized using conventional Schlenk-line techniques via a low-temperature hot-injection method[86]. For $AgBiS_2$ QD synthesis, 3.2 mmol of silver(I) acetate (Ag(OAc)), 4 mmol of bismuth(III) acetate ($Bi(OAc)_3$), 15 mL of 1-octadecene (ODE), and 24 mL of oleic acid (OA) were stirred under vacuum at 100 °C for 2 h to form Ag and Bi oleates. The reaction atmosphere was then switched to argon, and a solution of 4 mmol hexamethyldisilathiane (HMS) in 5 mL ODE was rapidly injected into the flask. The solution quickly turned dark brown, indicating the formation of $AgBiS_2$ QDs. The heating mantle was removed, and the reaction mixture was rapidly cooled using a cold-water bath. The crude solution was subsequently stirred at room temperature for 1 h. The QDs were isolated by ethanol addition followed by centrifugation[2].

6.2.2 Characterization of $AgBiS_2$ QDs

TEM characterizations were performed by dropping 10 µL of a 1 mM QD solution in toluene onto a copper support grid. TEM imaging was conducted using a HITACHI HF5000 200 kV (S)TEM. The UV–vis absorption spectra of QDs in solution were measured using a Shimadzu UV-3600 UV–vis–NIR spectrophotometer. XRD analysis of $AgBiS_2$ QDs was carried out using a Rigaku Miniflex 600 diffractometer with Cu Kα radiation ($\lambda = 1.54$ Å) at a scan rate of 5° per minute. QDs dispersed in toluene were deposited on 1 cm × 1 cm silicon wafers for XRD measurements; the samples were then heated at 70 °C for 30 min to evaporate the solvent.[87]

6.3 Chronoamperometry and Chronopotentiometry Measurements

Photoelectrochemical measurements were performed using an Autolab Potentiostat/Galvanostat PGSTAT (Metrohm, The Netherlands). The experiments were conducted under pulsed illumination provided by a red light-emitting diode (LED) source (Thorlabs, M780LP1). The optical power of the illumination was precisely monitored and adjusted using a calibrated optical power meter (Newport 843-R). All data acquisition and analysis were carried out using the NOVA software package.

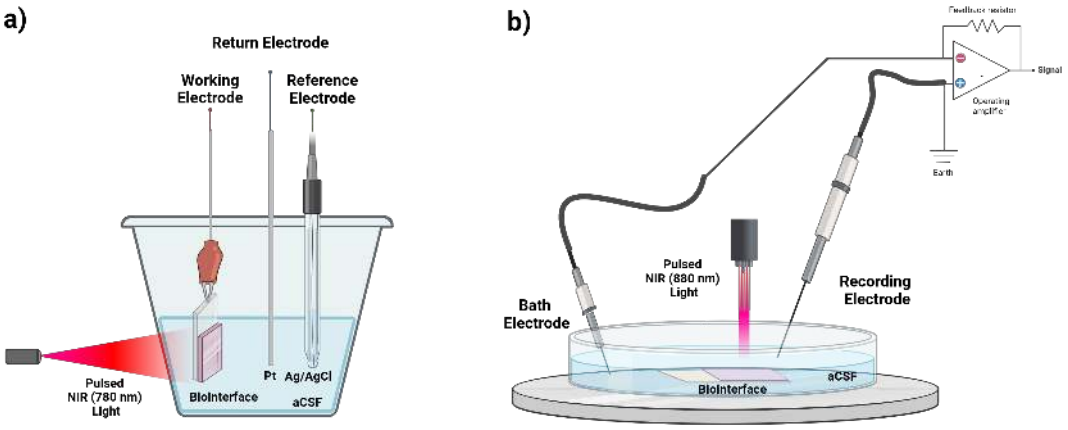

Figure 6.1: a) Photoelectrochemistry setup used for photovoltage and photocurrent characterization of the biointerface. b) Photocurrent measurement via patch-pipette tip positioned close to the surface of the biointerface.

6.4 Photocurrent Measurement

The measurements were performed using an Olympus T2 upright microscope in combination with EPC 800 extracellular patch clamp amplifiers (HEKA Elektronik GmbH, Pfalz, Germany). The modified artificial cerebrospinal fluid (aCSF) aqueous medium was prepared by dissolving 10 mM 4-(2-hydroxyethyl)-1-piperazineethanesulfonic acid (HEPES), 10 mM glucose, 2 mM $CaCl_2$, 140 mM NaCl, 1 mM $MgCl_2$, and 3 mM KCl in distilled water. The pH of the solution was adjusted to 7.4 using 1 M NaOH. Illumination was provided by a Thorlabs blue LED (M450LP1), which was operated using a DC2200 high-power single-channel LED driver with pulse modulation (Thorlabs Inc., NJ, USA). Photocurrent measurements were conducted with the ITO layer left electrically ungrounded, while the ground electrode was connected to the electrolyte solution to emulate biological conditions.

6.5 Primary Neuron Isolation and Culture

Primary hippocampal neuron isolation and culture protocols were performed according to our previous study[2].

6.5.1 Preparation of Substrates for Primary Neuron Culture

Each control ITO substrate and biointerface sample was rinsed with 70% ethanol and allowed to dry completely. The dried substrates were then placed in 6-well plates, followed by UV sterilization for 30 min under a cell culture hood. After sterilization, the substrates were coated with poly-L-lysine (PLL, Sigma-Aldrich, MO, USA) and incubated for 24 h at 37 °C in a humidified atmosphere containing 5% CO_2 to enhance cell adhesion. Upon completion of the incubation, the substrates were rinsed with Nanopure water and allowed to dry under the culture hood prior to seeding the primary neurons.

6.5.2 Primary Neuron Isolation

All experimental procedures were approved by the Institutional Animal Care and Use Committees of Koç University (Approval No: 2021.HADYEK.029) and conducted in accordance with Directive 2010/63/EU of the European Parliament and of the Council on the Protection of Animals Used for Scientific Purposes. For primary neuron isolation, hippocampal tissue was dissected from the brains of Wistar Albino rat embryos at embryonic days E16–E18. Immediately after dissection, the tissues were transferred into a Falcon tube containing ice-cold Hank's Balanced Salt Solution (HBSS). Following rinsing with ice-cold HBSS, the tissues were incubated in a 0.25% trypsin–EDTA solution supplemented with 2% DNase I in a Falcon tube for 20 min at 37 °C to initiate enzymatic digestion. During incubation, the tube was gently rotated up and down 2–3 times to improve digestion efficiency.

To stop the enzymatic reaction, Dulbecco's Modified Eagle Medium/Nutrient Mixture F-12 (DMEM/F12) supplemented with 10% fetal bovine serum (FBS) and 1% penicillin/streptomycin was added. The tissue suspension was then centrifuged at 300 g for 3 min. The supernatant containing DMEM/F12 was carefully removed and replaced with Neurobasal Plus medium (NBM) supplemented with B27, L-glutamine, β-mercaptoethanol, glutamate, and 1% penicillin/streptomycin. The cell pellet resuspended in NBM was continuously triturated using a plastic Pasteur pipette until no large tissue fragments were visible. The resulting homogeneous cell suspension was passed through a 70 μm cell strainer into a new Falcon tube.

Cells collected in the Falcon tube were seeded onto each poly-L-lysine-coated control ITO and biointerface substrate and maintained in a cell culture incubator at 37 °C with 5% CO_2 for 3 days. On the third day, half of the culture medium was replaced with NBM supplemented with cytosine arabinoside to inhibit glial cell overgrowth. After an additional 24 h of incubation, all culture medium was replaced with complete Neurobasal Medium supplemented with B27, L-glutamine, and 1% penicillin/streptomycin to prepare the substrates for subsequent experiments. For extended culture periods, half of the medium was refreshed every 3–4 days.

6.6 Biocompatibility Assays

Biocompatibility tests were performed according to our previous study[1, 2].

6.6.1 Cell-Titer Glo Toxicity Assay

Cell viability on ITO and $AgBiS_2$ biointerfaces was evaluated using the CellTiter-Glo Luminescent Cell Viability Assay (CTG, Promega, Mannheim, Germany), which quantifies adenosine triphosphate (ATP) as an indicator of metabolically active cells. Primary neurons (500,000 cells/well) were cultured on the substrates for three days. On day in vitro 3 (DIV3), half of the medium was replaced with neurobasal medium (NBM) supplemented with cytosine arabinoside to suppress glial proliferation, as previously described. After 24 h, the medium was exchanged with complete NBM, and viability testing was performed on DIV5.

Before the assay, the substrates were equilibrated at room temperature for 30 min, after which CellTiter-Glo reagent was applied. Samples were placed on an orbital shaker for 5 min and incubated for 10 min at room temperature. The resulting lysates were transferred to a 96-well opaque plate, and luminescence signals were recorded using a Synergy H1 Microplate Reader (Bio-Tek Instruments). Relative viability on the $AgBiS_2$ biointerface was quantified by comparison with the ITO control.

6.6.2 Immunofluorescence Staining and Imaging

Primary hippocampal neurons were cultured on ITO controls and $AgBiS_2$ biointerface substrates at a density of 500,000 cells/well, as previously described. On day 0, cells were fixed with ice-cold 4% paraformaldehyde in PBS for 20 min and rinsed three times with PBS-T (PBS containing 0.1% Tween-20). Permeabilization was performed by incubating with 0.1% Triton X-100 in PBS for 8 min, followed by blocking with Superblock (Thermo Fisher Scientific, MA, USA) for 10 min at room temperature.

To evaluate neuronal morphology and expression of neuronal markers, samples were incubated overnight with anti-NeuN antibody (ab177487, Abcam, Cambridge,

UK) and anti-beta-III tubulin antibody (ab18207, Abcam, Cambridge, UK) diluted in blocking solution. After washing with PBS-T, the cells were incubated with goat anti-rabbit IgG H&L Alexa Fluor 488 secondary antibody (Cell Signaling Technology, MA, USA) for 90 min at 37 °C. Samples were then washed, mounted using DAPI-containing mounting medium (50001, Ibidi GmbH, Germany), and imaged using an inverted fluorescence microscope (Axio Observer Z1, ZEISS, Oberkochen, Germany). The same procedure was repeated for samples at day 14.

6.6.3 TUNEL Toxicity Test

Apoptotic cell death was assessed using the TUNEL assay (Abcam, ab66110), which enables the evaluation of cell viability at the cellular and tissue levels through immunofluorescent labeling. Primary neurons were seeded on tandem biointerface substrates and ITO control substrates at a density of 500,000 cells per sample and incubated for 48 h. Cells were then fixed with 4% paraformaldehyde and washed three times with PBS-T (PBS containing 0.1% Triton X-100).

For combined TUNEL and beta-III tubulin staining, samples were first processed for beta-III tubulin labeling as described in the Immunofluorescence section. After three 5-minute PBS washes, the cells were treated with the wash solution provided in the TUNEL kit for 10 min at room temperature. DNA labeling solution was then applied for 1 h at 37 °C, followed by a 10-minute PBS wash and incubation with the antibody solution for 30 min at room temperature. The samples were rinsed with distilled water for 5 min, mounted with DAPI-containing medium, and imaged. Negative controls were processed in parallel. Imaging was performed using an inverted fluorescence microscope compatible with immunofluorescence (Axio Observer Z1, ZEISS, Oberkochen, Germany).

Chapter 7

CONCLUSION

This thesis presents the design, fabrication, and evaluation of a flexible homotandem photodiode based on $AgBiS_2$, aimed at serving as a high-efficiency optoelectronic biointerface for neural photostimulation. The core idea explored here is the adaptation of a tandem device architecture—commonly utilized in photovoltaic systems—for application in biomedical devices, where it addresses key challenges such as limited voltage output and suboptimal charge injection typically encountered in single-junction photodiodes.

By connecting two $AgBiS_2$ subcells in series and introducing a thin gold interlayer for electrical interconnection, the tandem configuration achieved a substantial boost in photovoltage—approximately 60% higher than that of its single-junction counterpart. These improvements are consistent with both photoelectrochemical characterizations and J–V curve analyses discussed earlier in the thesis.

The increase in photovoltage had a direct impact on device performance under near-infrared (NIR) light conditions relevant to biological systems. Patch-clamp electrophysiology experiments showed that the tandem devices were capable of delivering higher charge densities even at relatively low light intensities, indicating enhanced capacitive stimulation efficiency. These results validate the effectiveness of tandem architectures in enabling reliable neural activation while operating within safe optical limits.

In vitro evaluations—including cell viability (CTG), immunostaining, and TUNEL assays—further confirmed that the device did not induce cytotoxic effects or morphological alterations in neurons, either in short- or long-term exposure scenarios. These findings collectively reinforce the biocompatibility of the full device stack.

Taken together, the research illustrates the strong potential of $AgBiS_2$ homotandem photodiodes as safe, efficient, and mechanically flexible interfaces for neural

stimulation. The improvements in both photovoltage and charge injection capacity suggest a promising direction for developing high-resolution, photovoltaic-based prosthetic systems and other implantable bioelectronic devices capable of operating under minimal illumination intensities.

Beyond demonstrating device functionality, the thesis contributes several practical advances: a scalable approach to device fabrication, optimization of the interlayer composition and absorber layer thickness, and a method for achieving current matching by adjusting solution concentrations during synthesis. These insights are not only relevant for neural interfaces but could also inform future work in the broader field of tandem photovoltaic device engineering.

Looking ahead, further research might target pixel array miniaturization, long-term biocompatibility in *in vivo* environments, and enhanced interfacial charge transfer efficiency. Integration with microelectrode arrays could help improve spatial precision in neural targeting. Additionally, tuning the photodiode's spectral sensitivity toward longer NIR wavelengths may offer benefits in terms of tissue penetration and safety, particularly for deeper or more sensitive implantable applications.

In summary, the outcomes of this work lay a strong foundation for the development of next-generation wireless neurostimulation systems. By leveraging tandem quantum-dot photodiode architectures, it is possible to significantly enhance device performance without compromising flexibility or biological safety—marking a significant step forward in the field of implantable bioelectronics, including retinal prostheses and peripheral nerve modulation technologies.

BIBLIOGRAPHY

[1] Onuralp Karatum, Humeyra Nur Kaleli, Guncem Ozgun Eren, Afsun Sahin, and Sedat Nizamoglu. Electrical stimulation of neurons with quantum dots via near-infrared light. *ACS Nano*, 16(5):8233–8243, 2022.

[2] Ridvan Balamur, Jae Taek Oh, Onuralp Karatum, Yongjie Wang, Asim Onal, Humeyra Nur Kaleli, Cigdem Pehlivan, Afsun Şahin, Murat Hasanreisoglu, Gerasimos Konstantatos, and Sedat Nizamoglu. Capacitive and efficient near-infrared stimulation of neurons via an ultrathin agbis2 nanocrystal layer. *ACS Applied Materials & Interfaces*, 16(23):29610–29620, 2024.

[3] A. Goyal, S. Goetz, S. Stanslaski, Y. Oh, A. E. Rusheen, B. Klassen, K. Miller, C. D. Blaha, K. E. Bennet, and K. Lee. The development of an implantable deep brain stimulation device with simultaneous chronic electrophysiological recording and stimulation in humans. *Biosens Bioelectron*, 176:112888, 2021.

[4] V. A. Pavlov and K. J. Tracey. Bioelectronic medicine: Preclinical insights and clinical advances. *Neuron*, 110(21):3627–3644, 2022.

[5] V. S. Mallela, V. Ilankumaran, and N. S. Rao. Trends in cardiac pacemaker batteries. *Indian Pacing Electrophysiol J*, 4(4):201–12, 2004.

[6] F. G. Zeng, S. Rebscher, W. Harrison, X. Sun, and H. Feng. Cochlear implants: system design, integration, and evaluation. *IEEE Rev Biomed Eng*, 1:115–42, 2008.

[7] D. T. Brocker and W. M. Grill. Principles of electrical stimulation of neural tissue. *Handb Clin Neurol*, 116:3–18, 2013.

[8] Sung Il Park, Daniel S. Brenner, Gunchul Shin, Clinton D. Morgan, Bryan A. Copits, Ha Uk Chung, Melanie Y. Pullen, Kyung Nim Noh, Steve Davidson,

Soong Ju Oh, Jangyeol Yoon, Kyung-In Jang, Vijay K. Samineni, Megan Norman, Jose G. Grajales-Reyes, Sherri K. Vogt, Saranya S. Sundaram, Kellie M. Wilson, Jeong Sook Ha, Renxiao Xu, Taisong Pan, Tae-il Kim, Yonggang Huang, Michael C. Montana, Judith P. Golden, Michael R. Bruchas, Robert W. Gereau, and John A. Rogers. Soft, stretchable, fully implantable miniaturized optoelectronic systems for wireless optogenetics. *Nature Biotechnology*, 33(12):1280–1286, 2015.

[9] A. M. Aravanis, L. P. Wang, F. Zhang, L. A. Meltzer, M. Z. Mogri, M. B. Schneider, and K. Deisseroth. An optical neural interface: in vivo control of rodent motor cortex with integrated fiberoptic and optogenetic technology. *J Neural Eng*, 4(3):S143–56, 2007.

[10] Mertcan Han, Erdost Yildiz, Hümeyra Nur Kaleli, Selcan Karaz, Guncem Ozgun Eren, Itir Bakis Dogru-Yuksel, Erkan Senses, Afsun Şahin, and Sedat Nizamoglu. Tissue-like optoelectronic neural interface enabled by pedot:pss hydrogel for cardiac and neural stimulation. *Advanced Healthcare Materials*, 11(8):2102160, 2022.

[11] A. N. Bashkatov, E. A. Genina, V. I. Kochubey, and V. V. Tuchin. Optical properties of human skin, subcutaneous and mucous tissues in the wavelength range from 400 to 2000 nm. *Journal of Physics D: Applied Physics*, 38(15):2543, 2005.

[12] D. Palanker, Y. Le Mer, S. Mohand-Said, and J. A. Sahel. Simultaneous perception of prosthetic and natural vision in amd patients. *Nat Commun*, 13(1):513, 2022.

[13] T. C. Pappas, W. M. Wickramanyake, E. Jan, M. Motamedi, M. Brodwick, and N. A. Kotov. Nanoscale engineering of a cellular interface with semiconductor nanoparticle films for photoelectric stimulation of neurons. *Nano Lett*, 7(2):513–9, 2007.

[14] D. R. Merrill, M. Bikson, and J. G. Jefferys. Electrical stimulation of ex-

citable tissue: design of efficacious and safe protocols. *J Neurosci Methods*, 141(2):171–98, 2005.

[15] L. Truong, I. S. Moody, D. P. Stankus, J. A. Nason, M. C. Lonergan, and R. L. Tanguay. Differential stability of lead sulfide nanoparticles influences biological responses in embryonic zebrafish. *Arch Toxicol*, 85(7):787–98, 2011.

[16] Mertcan Han, Houman Bahmani Jalali, Erdost Yildiz, Mohammad Haroon Qureshi, Afsun Şahin, and Sedat Nizamoglu. Photovoltaic neurointerface based on aluminum antimonide nanocrystals. *Communications Materials*, 2(1):19, 2021.

[17] K. Lugo, X. Miao, F. Rieke, and L. Y. Lin. Remote switching of cellular activity and cell signaling using light in conjunction with quantum dots. *Biomed Opt Express*, 3(3):447–54, 2012.

[18] O. Karatum, M. M. Aria, G. O. Eren, E. Yildiz, R. Melikov, S. B. Srivastava, S. Surme, I. B. Dogru, H. Bahmani Jalali, B. Ulgut, A. Sahin, I. H. Kavakli, and S. Nizamoglu. Nanoengineering inp quantum dot-based photoactive biointerfaces for optical control of neurons. *Front Neurosci*, 15:652608, 2021.

[19] Giulio Simone, Dario Di Carlo Rasi, Xander de Vries, Gaël H. L. Heintges, Stefan C. J. Meskers, René A. J. Janssen, and Gerwin H. Gelinck. Near-infrared tandem organic photodiodes for future application in artificial retinal implants. *Advanced Materials*, 30(51):1804678, 2018.

[20] Stuart F. Cogan. Neural stimulation and recording electrodes. *Annual Review of Biomedical Engineering*, 10(Volume 10, 2008):275–309, 2008.

[21] Sang Min Won, Enming Song, Jonathan T. Reeder, and John A. Rogers. Emerging modalities and implantable technologies for neuromodulation. *Cell*, 181(1):115–135, 2020.

[22] Bruce P. Bean. The action potential in mammalian central neurons. *Nature Reviews Neuroscience*, 8(6):451–465, 2007.

[23] Peter G Wirsing, Alexander D Habrom, Thomas M Zehnder, Sandra Friedli, and Marlise Blatti. Wireless micro current stimulation – an innovative electrical stimulation method for the treatment of patients with leg and diabetic foot ulcers. *International Wound Journal*, 12(6):693–698, 2015.

[24] Sang Min Won, Enming Song, Jianing Zhao, Jinghua Li, Jonathan Rivnay, and John A. Rogers. Recent advances in materials, devices, and systems for neural interfaces. *Advanced Materials*, 30(30):1800534, 2018.

[25] Huihua Xu, Lan Yin, Chuan Liu, Xing Sheng, and Ni Zhao. Recent advances in biointegrated optoelectronic devices. *Advanced Materials*, 30(33):1800156, 2018.

[26] Mertcan Han, Shashi Bhushan Srivastava, Erdost Yildiz, Rustamzhon Melikov, Saliha Surme, Itir Bakis Dogru-Yuksel, Ibrahim Halil Kavakli, Afsun Sahin, and Sedat Nizamoglu. Organic photovoltaic pseudocapacitors for neurostimulation. *ACS Applied Materials & Interfaces*, 12(38):42997–43008, 2020.

[27] Ingmar Schoen and Peter Fromherz. The mechanism of extracellular stimulation of nerve cells on an electrolyte-oxide-semiconductor capacitor. *Biophysical Journal*, 92(3):1096–1111, 2007.

[28] M. Jakesova, M. Silvera Ejneby, V. Derek, T. Schmidt, M. Gryszel, J. Brask, R. Schindl, D. T. Simon, M. Berggren, F. Elinder, and E. D. Glowacki. Optoelectronic control of single cells using organic photocapacitors. *Sci Adv*, 5(4):eaav5265, 2019.

[29] Lokman Kaya, Onuralp Karatum, Rıdvan Balamur, Hümeyra Nur Kaleli, Asım Önal, Sharadrao Anandrao Vanalakar, Murat Hasanreisoğlu, and Sedat Nizamoglu. Mno2 nanoflower integrated optoelectronic biointerfaces for photostimulation of neurons. *Advanced Science*, 10(25):2301854, 2023.

[30] C. Magariños-Ascone, J. H. Pazo, O. Macadar, and W. Buño. High-frequency stimulation of the subthalamic nucleus silences subthalamic neurons: a possible cellular mechanism in parkinson disease. *Neuroscience*, 115(4):1109–1117, 2002.

[31] Keyoumars Ashkan, Priya Rogers, Hagai Bergman, and Ismail Ughratdar. Insights into the mechanisms of deep brain stimulation. *Nature Reviews Neurology*, 13(9):548–554, 2017.

[32] Jung Min Lee, Dingchang Lin, Ha-Reem Kim, Young-Woo Pyo, Guosong Hong, Charles M. Lieber, and Hong-Gyu Park. All-tissue-like multifunctional optoelectronic mesh for deep-brain modulation and mapping. *Nano Letters*, 21(7):3184–3190, 2021.

[33] Xiang Wu, Yuyan Jiang, Nicholas J. Rommelfanger, Fan Yang, Qi Zhou, Rongkang Yin, Junlang Liu, Sa Cai, Wei Ren, Andrew Shin, Kyrstyn S. Ong, Kanyi Pu, and Guosong Hong. Tether-free photothermal deep-brain stimulation in freely behaving mice via wide-field illumination in the near-infrared-ii window. *Nature Biomedical Engineering*, 6(6):754–770, 2022.

[34] Naïg Aurelia Ludmilla Chenais, Marta Jole Ildelfonsa Airaghi Leccardi, and Diego Ghezzi. Photovoltaic retinal prosthesis restores high-resolution responses to single-pixel stimulation in blind retinas. *Communications Materials*, 2(1):28, 2021.

[35] Marta Jole Ildelfonsa Airaghi Leccardi, Naïg Aurelia Ludmilla Chenais, Laura Ferlauto, Maciej Kawecki, Elodie Geneviève Zollinger, and Diego Ghezzi. Photovoltaic organic interface for neuronal stimulation in the near-infrared. *Communications Materials*, 1(1):21, 2020.

[36] Keith Mathieson, James Loudin, Georges Goetz, Philip Huie, Lele Wang, Theodore I. Kamins, Ludwig Galambos, Richard Smith, James S. Harris, Alexander Sher, and Daniel Palanker. Photovoltaic retinal prosthesis with high pixel density. *Nature Photonics*, 6(6):391–397, 2012.

[37] Paola Vagni, Marta Jole Ildelfonsa Airaghi Leccardi, Charles-Henri Vila, Elodie Geneviève Zollinger, Golnaz Sherafatipour, Thomas J. Wolfensberger, and Diego Ghezzi. Polyretina restores light responses in vivo in blind göttingen minipigs. *Nature Communications*, 13(1):3678, 2022.

[38] Bing-Yi Wang, Zhijie Charles Chen, Mohajeet Bhuckory, Tiffany Huang, Andrew Shin, Valentina Zuckerman, Elton Ho, Ethan Rosenfeld, Ludwig Galambos, Theodore Kamins, Keith Mathieson, and Daniel Palanker. Electronic photoreceptors enable prosthetic visual acuity matching the natural resolution in rats. *Nature Communications*, 13(1):6627, 2022.

[39] E. Castagnola, L. Maiolo, E. Maggiolini, A. Minotti, M. Marrani, F. Maita, A. Pecora, G. N. Angotzi, A. Ansaldo, M. Boffini, L. Fadiga, G. Fortunato, and D. Ricci. Pedot-cnt-coated low-impedance, ultra-flexible, and brain-conformable micro-ecog arrays. *IEEE Transactions on Neural Systems and Rehabilitation Engineering*, 23(3):342–350, 2015.

[40] Yanna Sun, Tao Liu, Yuanyuan Kan, Ke Gao, Bo Tang, and Yuliang Li. Flexible organic solar cells: Progress and challenges. *Small Science*, 1(5):2100001, 2021.

[41] Seongjun Park, Gabriel Loke, Yoel Fink, and Polina Anikeeva. Flexible fiber-based optoelectronics for neural interfaces. *Chemical Society Reviews*, 48(6):1826–1852, 2019.

[42] Laura Ferlauto, Marta Jole Ildelfonsa Airaghi Leccardi, Naïg Aurelia Ludmilla Chenais, Samuel Charles Antoine Gilliéron, Paola Vagni, Michele Bevilacqua, Thomas J. Wolfensberger, Kevin Sivula, and Diego Ghezzi. Design and validation of a foldable and photovoltaic wide-field epiretinal prosthesis. *Nature Communications*, 9(1):992, 2018.

[43] Malin Silvera Ejneby, Marie Jakesova, Jose J. Ferrero, Ludovico Migliaccio, Ihor Sahalianov, Zifang Zhao, Magnus Berggren, Dion Khodagholy, Vedran Derek, Jennifer N. Gelinas, and Eric Daniel Glowacki. Chronic electrical stimulation of peripheral nerves via deep-red light transduced by an implanted organic photocapacitor. *Nature Biomedical Engineering*, 6(6):741–753, 2022.

[44] Houman Bahmani Jalali, Onuralp Karatum, Rustamzhon Melikov, Ugur Meric Dikbas, Sadra Sadeghi, Erdost Yildiz, Itir Bakis Dogru, Guncem Ozgun Eren, Cagla Ergun, Afsun Sahin, Ibrahim Halil Kavakli, and Sedat Nizamoglu.

Biocompatible quantum funnels for neural photostimulation. *Nano Letters*, 19(9):5975–5981, 2019.

[45] Sandra J. Rosenthal, Jerry C. Chang, Oleg Kovtun, James R. McBride, and Ian D. Tomlinson. Biocompatible quantum dots for biological applications. *Chemistry & Biology*, 18(1):10–24, 2011.

[46] Mertcan Han, Onuralp Karatum, and Sedat Nizamoglu. Optoelectronic neural interfaces based on quantum dots. *ACS Applied Materials & Interfaces*, 14(18):20468–20490, 2022.

[47] Onuralp Karatum, Guncem Ozgun Eren, Rustamzhon Melikov, Asim Onal, Cleva W. Ow-Yang, Mehmet Sahin, and Sedat Nizamoglu. Quantum dot and electron acceptor nano-heterojunction for photo-induced capacitive charge-transfer. *Scientific Reports*, 11(1):2460, 2021.

[48] Kostas Kostarelos, Melissa Vincent, Clement Hebert, and Jose A. Garrido. Graphene in the design and engineering of next-generation neural interfaces. *Advanced Materials*, 29(42):1700909, 2017.

[49] Hyunsu Park, Pavel Takmakov, and Hyowon Lee. Electrochemical evaluations of fractal microelectrodes for energy efficient neurostimulation. *Scientific Reports*, 8(1):4375, 2018.

[50] Anton V. Volkov, Kosala Wijeratne, Evangelia Mitraka, Ujwala Ail, Dan Zhao, Klas Tybrandt, Jens Wenzel Andreasen, Magnus Berggren, Xavier Crispin, and Igor V. Zozoulenko. Understanding the capacitance of pedot:pss. *Advanced Functional Materials*, 27(28):1700329, 2017.

[51] William Shockley and Hans J. Queisser. Detailed Balance Limit of Efficiency of *p-n* Junction Solar Cells. *Journal of Applied Physics*, 32(3):510–519, 1961.

[52] A De Vos. Detailed balance limit of the efficiency of tandem solar cells. *Journal of Physics D: Applied Physics*, 13(5):839–846, 1980.

[53] Shu-Guang Meng, Xiao-Zhao Zhu, Dong-Ying Zhou, and Liang-Sheng Liao. Recent Progresses in Solution-Processed Tandem Organic and Quantum Dots Light-Emitting Diodes. *Molecules*, 28(1):134, 2022.

[54] Juncheng Zhu, Kunyuan Lu, Jing Li, Zeke Liu, and Wanli Ma. Tandem solar cells based on quantum dots. *Materials Chemistry Frontiers*, 8(7):1792–1807, 2024.

[55] Tomas Leijtens, Kevin A. Bush, Rohit Prasanna, and Michael D. McGehee. Opportunities and challenges for tandem solar cells using metal halide perovskite semiconductors. *Nature Energy*, 3(10):828–838, 2018.

[56] Xingliang Li, Qiaojing Xu, Lingling Yan, Chengchao Ren, Biao Shi, Pengyang Wang, Sayantan Mazumdar, Guofu Hou, Ying Zhao, and Xiaodan Zhang. Silicon heterojunction-based tandem solar cells: past, status, and future prospects. *Nanophotonics*, 10(8):2001–2022, 2021.

[57] Shangshang Chen, Guangye Zhang, Jing Liu, Huatong Yao, Jianquan Zhang, Tingxuan Ma, Zhengke Li, and He Yan. An All-Solution Processed Recombination Layer with Mild Post-Treatment Enabling Efficient Homo-Tandem Non-fullerene Organic Solar Cells. *Advanced Materials*, 29(6):1604231, 2017.

[58] Yangqin Gao, Vincent M. Le Corre, Alexandre Gaïtis, Marios Neophytou, Mahmoud Abdul Hamid, Kazuhiro Takanabe, and Pierre M. Beaujuge. Homo-Tandem Polymer Solar Cells with V_{oc} >1.8 V for Efficient PV-Driven Water Splitting. *Advanced Materials*, 28(17):3366–3373, 2016.

[59] Huiqiong Zhou, Yuan Zhang, Cheng-Kang Mai, Samuel D. Collins, Guillermo C. Bazan, Thuc-Quyen Nguyen, and Alan J. Heeger. Polymer Homo-Tandem Solar Cells with Best Efficiency of 11.3%. *Advanced Materials*, 27(10):1767–1773, 2015.

[60] Kirstin Alberi, Joseph J. Berry, Jacob J. Cordell, Daniel J. Friedman, John F. Geisz, Ahmad R. Kirmani, Bryon W. Larson, William E. McMahon,

Lorelle M. Mansfield, Paul F. Ndione, Michael Owen-Bellini, Axel F. Palmstrom, Matthew O. Reese, Samantha B. Reese, Myles A. Steiner, Adele C. Tamboli, San Theingi, and Emily L. Warren. A roadmap for tandem photovoltaics. *Joule*, 8(3):658–692, 2024.

[61] Lingxian Meng, Yamin Zhang, Xiangjian Wan, Chenxi Li, Xin Zhang, Yanbo Wang, Xin Ke, Zuo Xiao, Liming Ding, Ruoxi Xia, Hin-Lap Yip, Yong Cao, and Yongsheng Chen. Organic and solution-processed tandem solar cells with 17.3% efficiency. *Science*, 361(6407):1094–1098, 2018.

[62] Donggu Lee, Wan Ki Bae, Insun Park, Do Y. Yoon, Seonghoon Lee, and Changhee Lee. Transparent electrode with ZnO nanoparticles in tandem organic solar cells. *Solar Energy Materials and Solar Cells*, 95(1):365–368, 2011.

[63] Meng Zhang and Zhiqun Lin. Efficient interconnecting layers in monolithic all-perovskite tandem solar cells. *Energy & Environmental Science*, 15(8):3152–3170, 2022.

[64] C.H.Y. Ho, J. Kothari, X. Fu, and F. So. Interconnecting layers for tandem organic solar cells. *Materials Today Energy*, 21:100707, 2021.

[65] Ramakrishna Madaka, Dinesh Kumar, Ashish K. Singh, Md. Seraj Uddin, and Jatin Kumar Rath. Tunnel recombination junction influence on the a-Si:H/SHJ tandem solar cell. *Materials Today: Proceedings*, 39:1970–1973, 2021.

[66] Zhenzhen Shi, Yiming Bai, Xiaohan Chen, Rui Zeng, and Zhan'ao Tan. Tandem structure: a breakthrough in power conversion efficiency for highly efficient polymer solar cells. *Sustainable Energy & Fuels*, 3(4):910–934, 2019.

[67] Jingjing Tian, Chao Liu, Karen Forberich, Anastasia Barabash, Zhiqiang Xie, Shudi Qiu, Jiwon Byun, Zijian Peng, Kaicheng Zhang, Tian Du, Sanjayan Sathasivam, Thomas J. Macdonald, Lirong Dong, Chaohui Li, Jiyun Zhang, Marcus Halik, Vincent M. Le Corre, Andres Osvet, Thomas Heumüller, Ning Li, Yinhua Zhou, Larry Lüer, and Christoph J. Brabec. Overcoming optical

losses in thin metal-based recombination layers for efficient n-i-p perovskite-organic tandem solar cells. *Nature Communications*, 16(1):154, 2025.

[68] Jianghui Zheng, Cho Fai Jonathan Lau, Hamid Mehrvarz, Fa-Jun Ma, Yajie Jiang, Xiaofan Deng, Anastasia Soeriyadi, Jincheol Kim, Meng Zhang, Long Hu, Xin Cui, Da Seul Lee, Jueming Bing, Yongyoon Cho, Chao Chen, Martin A. Green, Shujuan Huang, and Anita W. Y. Ho-Baillie. Large area efficient interface layer free monolithic perovskite/homo-junction-silicon tandem solar cell with over 20% efficiency. *Energy & Environmental Science*, 11(9):2432–2443, 2018.

[69] Maximilian T. Hörantner, Tomas Leijtens, Mark E. Ziffer, Giles E. Eperon, M. Greyson Christoforo, Michael D. McGehee, and Henry J. Snaith. The Potential of Multijunction Perovskite Solar Cells. *ACS Energy Letters*, 2(10):2506–2513, 2017.

[70] Ryan W. Crisp, Gregory F. Pach, J. Matthew Kurley, Ryan M. France, Matthew O. Reese, Sanjini U. Nanayakkara, Bradley A. MacLeod, Dmitri V. Talapin, Matthew C. Beard, and Joseph M. Luther. Tandem Solar Cells from Solution-Processed CdTe and PbS Quantum Dots Using a ZnTe–ZnO Tunnel Junction. *Nano Letters*, 17(2):1020–1027, 2017.

[71] Selina Kern, Gyusang Yi, Pascal Büttner, Florian Scheler, Minh-Hoa Tran, Sofia Korenko, Katharina E. Dehm, Ivan Kundrata, Achim Zahl, Steve Albrecht, Julien Bachmann, and Ryan W. Crisp. Monolithic two-terminal tandem solar cells using sb_2s_3 and solution-processed pbs quantum dots achieving an open-circuit potential beyond 1.1 v. *ACS Applied Materials & Interfaces*, 16(11):13903–13913, 2024.

[72] D. B Niranjan, Jennifer Jacob, B. R Vaidehi, Mathew Peter, Jeevan Medikonda, and Pramod K. Namboothiri. Current status and applications of photovoltaic technology in wearable sensors: a review. *Frontiers in Nanotechnology*, 5:1268931, 2023.

[73] Naureen, Sadanand, Shambhavi Rai, R. K. Yadav, Pooja Lohia, and D. K. Dwivedi. A simulation study of quantum dot solar cells using two distinct ETL of WO3 and WS2. *Optical and Quantum Electronics*, 55(6):541, 2023.

[74] Sandeep Kumar, Pragya Bharti, and Basudev Pradhan. Performance optimization of efficient pbs quantum dots solar cells through numerical simulation. *Scientific Reports*, 13(1):10511, 2023.

[75] Mojeed A. Agoro, Edson L. Meyer, and Olufemi I. Olayiwola. Fabrication of heterostructure multilayer devices through the optimization of Bi-metal sulfides for high-performance quantum dot-sensitized solar cells. *RSC Advances*, 14(46):33751–33763, 2024.

[76] Chia-Hao M. Chuang, Patrick R. Brown, Vladimir Bulović, and Moungi G. Bawendi. Improved performance and stability in quantum dot solar cells through band alignment engineering. *Nature Materials*, 13(8):796–801, 2014.

[77] Shailesh Narain Sharma, Pooja Semalti, Bhawna, and A. Srinivas Rao. Pioneering advancements in quantum dot solar cells: Innovations in synthesis and cutting-edge applications. *Current Opinion in Colloid & Interface Science*, 77:101905, 2025.

[78] Jagannathan Thirumalai, editor. *Quantum Dots - Recent Advances, New Perspectives and Contemporary Applications*. IntechOpen, 2023.

[79] Zhenyu Yang, James Z. Fan, Andrew H. Proppe, F. Pelayo García De Arquer, David Rossouw, Oleksandr Voznyy, Xinzheng Lan, Min Liu, Grant Walters, Rafael Quintero-Bermudez, Bin Sun, Sjoerd Hoogland, Gianluigi A. Botton, Shana O. Kelley, and Edward H. Sargent. Mixed-quantum-dot solar cells. *Nature Communications*, 8(1):1325, 2017.

[80] Qian Dong, Huiyan Liu, Yukihiro Hara, Hannah E. Starr, Jillian L. Dempsey, and Rene Lopez. Impact of Background Oxygen Pressure on the Pulsed-Laser Deposition of ZnO Nanolayers and on Their Corresponding Performance as

Electron Acceptors in PbS Quantum-Dot Solar Cells. *ACS Applied Nano Materials*, 2(2):767–777, 2019.

[81] Alina Senina, Anatol Prudnikau, Angelika Wrzesińska-Lashkova, Yana Vaynzof, and Fabian Paulus. Cation exchange synthesis of $AgBiS_2$ quantum dots for highly efficient solar cells. *Nanoscale*, 16(19):9325–9334, 2024.

[82] Cibrán López, Seán R. Kavanagh, Pol Benítez, Edgardo Saucedo, Aron Walsh, David O. Scanlon, and Claudio Cazorla. Chalcogen Vacancies Rule Charge Recombination in Pnictogen Chalcohalide Solar-Cell Absorbers. *ACS Energy Letters*, 10(7):3562–3569, 2025.

[83] Il Jeon, James W. Ryan, Tafu Nakazaki, Kee Sheng Yeo, Yuichi Negishi, and Yutaka Matsuo. Air-processed inverted organic solar cells utilizing a 2-aminoethanol-stabilized ZnO nanoparticle electron transport layer that requires no thermal annealing. *J. Mater. Chem. A*, 2(44):18754–18760, 2014.

[84] Fei Qin, Wen Wang, Lulu Sun, Xueshi Jiang, Lin Hu, Sixing Xiong, Tiefeng Liu, Xinyun Dong, Jing Li, Youyu Jiang, Jianhui Hou, Kenjiro Fukuda, Takao Someya, and Yinhua Zhou. Robust metal ion-chelated polymer interfacial layer for ultraflexible non-fullerene organic solar cells. *Nature Communications*, 11(1):4508, 2020.

[85] Gomaa Mohamed Gomaa Khalaf, Xinzhao Zhao, Mingyu Li, Chunxia Li, Salman Ali, Tianjun Ma, Hsien-Yi Hsu, Jianbin Zhang, and Haisheng Song. Efficient PbS quantum dots tandem solar cells through compatible interconnection layer. *Journal of Energy Chemistry*, 98:47–57, 2024.

[86] María Bernechea, Nichole Cates, Guillem Xercavins, David So, Alexandros Stavrinadis, and Gerasimos Konstantatos. Solution-processed solar cells based on environmentally friendly AgBiS2 nanocrystals. *Nature Photonics*, 10(8):521–525, 2016.

[87] Omer Faruk Ozelci, Humeyra Nur Kaleli, Tarik Safa Kaya, Gizem Yildiz, Melike Oztopal, Ebru Sarıoğlu, Ender Ödemiş, Erkan Senses, and Sedat Nizamoglu.

Hydrogel-Integrated Quantum Dot Biointerfaces for Near-Infrared Cardiac Photostimulation. *Advanced Functional Materials*, page e13988, 2025.